We are IntechOpen, the world's leading publisher of Open Access books
Built by scientists, for scientists

4,800
Open access books available

122,000
International authors and editors

135M
Downloads

154
Countries delivered to

Our authors are among the

TOP 1%
most cited scientists

12.2%
Contributors from top 500 universities

BOOK CITATION INDEX
CLARIVATE ANALYTICS
INDEXED

WEB OF SCIENCE™

Selection of our books indexed in the Book Citation Index
in Web of Science™ Core Collection (BKCI)

Interested in publishing with us?
Contact book.department@intechopen.com

Numbers displayed above are based on latest data collected.
For more information visit www.intechopen.com

Solution Processing of Nanoceramic VO$_2$ Thin Films for Application to Smart Windows

Yanfeng Gao[1,2,3,], Litao Kang[1], Zhang Chen[1] and Hongjie Luo[2]
[1]State Key Laboratory of High Performance Ceramics and Superfine Microstructure,
Shanghai institute of Ceramics, Chinese Academy of Sciences, Shanghai,
[2]Research Center for Industrial Ceramics, Shanghai institute of Ceramics,
Chinese Academy of Sciences, Shanghai,
[3]Xinjiang Key Laboratory of Electronic Information Materials and Devices,
Xinjiang Technical Institute of Physics & Chemistry, Chinese Academy of Sciences,
Beijing Road, Urumqi, Xinjiang,
China

1. Introduction

Energy conservation has directed a global trend towards sustainable development. Due to global warming, air conditioning systems have been widely used in daily life, thus inducing a series of problems,[1] including increases in electricity consumption and carbon dioxide emissions along with the formation of other atmospheric pollutants from the electricity-generation process. Air conditioning in China accounts for 40-60% of a building's energy consumption (the exact figure depends on the area of the building), and overall, uses 28% of the total available primary energy. These figures will grow rapidly with urban development, as the case of China. One effective way to reduce the amount of electricity consumed by cooling is to apply solar-control coatings to glass windows, or so-called "energy-efficient windows" or "smart windows". Because lighting demands transparency, most of the smart windows are designed to intelligently control the amount of light and heat (mainly in the near infrared region) passing through in response to an external stimulus such as light (photochromic), heat (thermochromic) or electricity (electrochromic).[2-7] In this regard, the thermochromic smart window, typically based on a vanadium dioxide (VO$_2$) functional layer, has received particular interests due to two aspects. First, it can respond to environmental temperatures, making reversible structural changes from an infrared-transparent semiconductive crystalline phase to an infrared-blocking metallic crystalline phase. Second, the visible transparency remains almost unchangeable.

VO$_2$, which undergoes a metal-insulator transition (MIT) at a critical temperature T$_c$ (68 °C for bulk VO$_2$),[8] has attracted much attention as a thermochromic material for smart windows.[9] Owing to the MIT, VO$_2$ transforms between the monoclinic (P2$_1$/c, M$_1$) and the tetragonal (P4$_2$/mnm, R) phase, inducing a severe change in optical properties. VO$_2$ is transparent to near infrared (NIR) light at temperatures below T$_c$, but NIR-light reflective above T$_c$. The MIT is simply determined by environmental temperature and occurs fast,

usually within 10^{-12} s (1 ps).[10-14] This character can be employed to intelligently control the NIR-light radiation which carries appropriate 45% heat energy of solar light, and makes VO_2 a promising material for smart windows. Though VO_2 single crystals cannot withstand the structural distortions associated with the MIT and break after a few cycles of the phase transition, VO_2 films can survive stress changes above 10^8 cycles[15-17] and thus is suitable for applications in smart windows.

However, an expensive fabrication method, low visible transparency and insufficient energy-saving efficiency limit the application of VO_2 smart windows to certain architectures. The difficulties in the VO_2 synthesis are due partially to the existence of abundant oxide forms and polymorphous of the vanadium-oxygen system. From the vanadium-oxygen phase-diagram, there are nearly 15 to 20 other stable vanadium oxide phases besides VO_2, such as VO, V_6O_{13}, and V_7O_{13}. The formation of VO_2 occurs only at a very narrow oxygen partial pressure of 2 (± 0.2) %.[18,19]

Additionally, more than ten kinds of crystalline phases of vanadium dioxide have been reported, including tetragonal rutile-type VO_2 (R) ($P4/mmm$),[20] monoclinic rutile-type VO_2 (M) ($P21/c$),[21] triclinic VO_2 ($P*(2)$),[22] tetragonal VO_2 (A) ($P42/nmc$),[23-25] monoclinic VO_2 (B) ($C2/m$),[26] (C) VO_2,[27] orthorhombic $VO_2 \cdot H_2O$ ($P222$),[28] tetragonal $VO_2 \cdot 0.5H_2O$ ($I4/mmm$),[29] monoclinic V_2O_4 ($P21/c$,), and $V_2O_4 \cdot 2H_2O$. Only the rutile-type VO_2 (R/M) undergoes a fully reversible metal-semiconductor phase transition (MST) at approximately 68 °C.

The low visible transmittance originates from the strong inner-band and inter-band absorptions in the short-wavelength range for both the metallic and semiconductive states.[30,31] The transmittance values in the visible region (380-780 nm) reported for VO_2 thin films are quite low (~50%,[32,33] 42-45 %,[34,35] or less than 40%[19,36-39]). However, for films suitable for use in architectural windows, the visible transmittance should exceed 60%.[40,41]

Energy-saving efficiency is one of limits that drawback the application of this material. For smart window applications, the optical characteristics of VO_2 films in the wavelength ranging from near-infrared (NIR) to mid-infrared are usually concerned.[34,38,42-45] The change in NIR transmittance before and after the MIT is defined as NIR switching efficiency (ΔT) of VO_2 films (typically referred to the transmission difference at a wavelength of 2000 nm), and this value is affected by several factors, for example film thickness,[45,46] doping,[36,47] microstructure[44,48,49] and stoichiometry.[50,51] Of these factors, the thickness usually affects the switching efficiency most dramatically, but increases in the thickness are usually accompanied by great losses in the visible transmittance.[46] For example, when the NIR switching efficiency reached 50%, the visible transmittance maxima were lowered to <43%,[52] <40%,[35] ~33%,[46] and ~21%,[53] respectively. Furthermore, to our knowledge, a NIR switching efficiency of 50% cannot even be achieved by increasing the film thickness.[36,51] The film becomes a static absorber if the thickness exceeds a threshold, without significant benefits on the NIR switching efficiency. In addition, the optical performance in the mid-infrared region, e.g., the contrast of both reflectance and emissivity before and after the MIT, is also highly concerned.[42,45]

The main preparation methods for VO_2 films are based on gas-phase reactions such as sputtering deposition,[4,5] chemical vapour deposition,[32,54] pulsed laser deposition[55] and ion implantation.[56] These methods are superior in terms of precise control of process parameters such as oxygen partial pressure (typically in the range of 0.06-0.13 Pa) and film features, including thickness and microstructure.[57,58] They are, however, restricted by expensive equipment. The low visible transmittance (integral transmittance≤40%) of VO_2 films originates from strong absorption and high reflectance.[36,59] Switching efficiency (ΔT_{sol}) refers

to a difference in the solar energy transmittance across metal-insulator transition (MIT) and is used to characterize the thermochromic properties of VO$_2$ films. This value is usually below 10% for a single layered VO$_2$ film.[4-5]

In the past several years, we have worked to develop a solution-based process for VO$_2$-based thin films with a special emphasis on their preparation, thermochromic property study and application to smart windows.[43,44,60-72] Polymer-assisted deposition (PAD) process was realized for the preparation of VO$_2$ and VO$_2$-based multilayered films. The method enables us to facially control over the film thickness, morphology and optical constants. By combining clever control of the optical parameters and/or their thickness and microstructural regulation, we obtained VO$_2$ films with high visible transmittance (40-84%), controllable Mott phase transition temperatures and high switching efficiencies (max. 15.1%). The results show that the current solution process is a powerful competitor towards practical applications of this material.

2. Polymer-assisted deposition of VO$_2$ films

2.1 The method

The process was started with vanadium oxides or inorganic salts, as shown in **Figure** 1. These raw materials were treated to make an aqueous transparent solution. To the above solution the selected, weighed soluble polymers and doping agents were added. Then the precursor VO$_2$ film was prepared by traditional solution methods, such as spinning coating or dip coating. After drying at 80 °C in air, the precursor film was annealed at 300- 600 °C in N$_2$. Readers can read references for details.[43,44]

It is also found that precursor solution without polyvinylpyrrolidone (PVP) was unstable and a large amount of precipitates formed after aging for several days. Whereas, PVP-employing solution stayed stable for several months with only a little precipitates suspending in the solution, indicating that PVP improved stability of the precursor solution, probably because the negatively charged carbonyl groups bound with aqua vanadium ions to form a relatively stable precursor solution.

To examine the interactions between PVP and aqua vanadium ions, Fourier transform infrared spectroscopy (FTIR) was employed to characterize the precursor solution with or without PVP. The results were shown in **Figure** 2. To compare, FTIR spectra of PVP (**Figure** 2a) and PVP in the presence of H$_2$SO$_4$ (**Figure** 2b) were also included. Generally, the strong and sharp peak at 1654 cm^{-1} was assigned to the stretching vibration of –C=O, and the peak at 1292 cm^{-1} was attributed to –C-N (**Figure** 2a).[73] When H$_2$SO$_4$ was added to PVP (**Figure** 2b), the stretching vibration of –C=O shifted to low wavenumber of 1635 cm^{-1}, which originates from the loosening of the –C=O double bond by coordinating between negatively charged carbonyl groups and H$^+$.[74] For precursor solution with PVP (**Figure** 2c), the frequency of –C=O stretching vibration became lower (1620 cm^{-1}) due to the influence of aqua vanadium ions. The coordination interactions between the carboxyl group of PVP and metal ions (Li, Ca, Co, Ag) were also reported in PVP–DMF–MCl$_n$ systems[75] as well as polymer/silver salt complex membranes.[76-78] Although the vibration at 1624 cm^{-1} in the spectrum for a PVP-free precursor solution was poorly identified (**Figure** 2d), the vibration of –C-N kept almost unchanged (**Figure** 2a, b and c) for all these films, indicating that there were no interactions between amine groups and aqua vanadium ions. According to above discussion, the effects of PVP on stabilizing precursor solution were due to the interactions of the negatively charged carbonyl groups in PVP with qua vanadium ions. Furthermore, it

is reported that the interactions between metal ions and the carbonyl groups from different PVP molecules increased the apparent viscosity of the PVP–DMF–MCl$_n$ solution (M = Li, Ca, Co),[75] where metal ions act as cross-linking points between different PVP molecular chains,[75] improving the film formability.
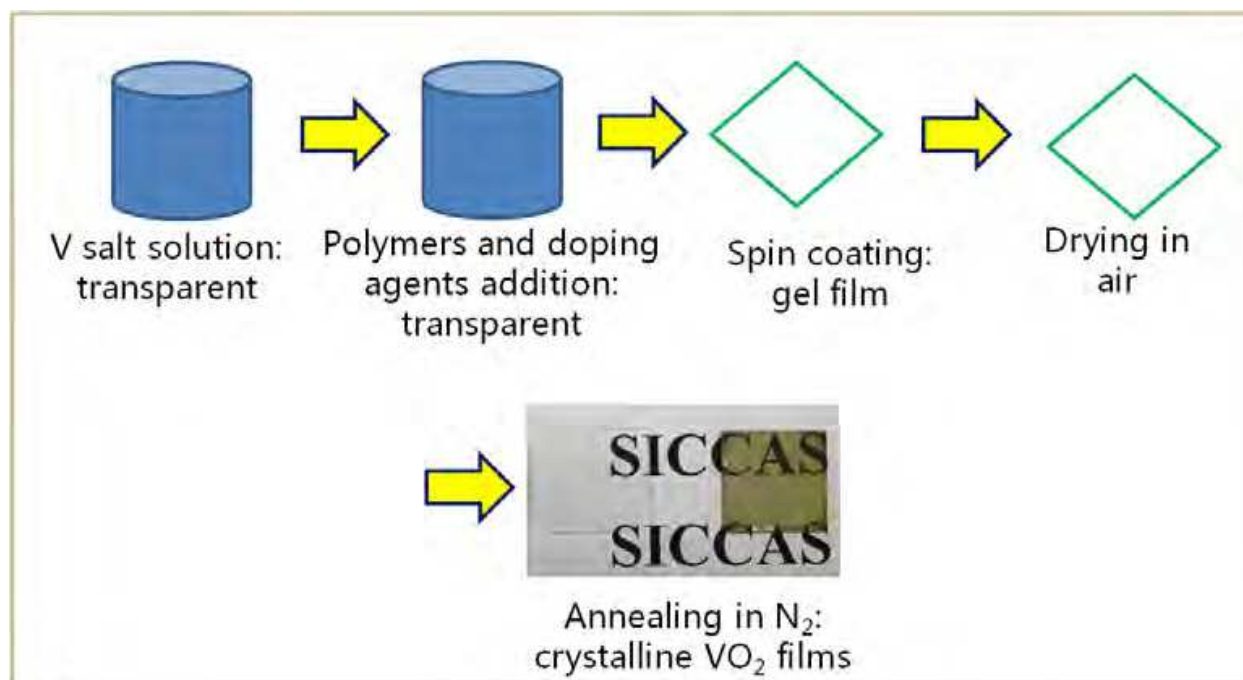

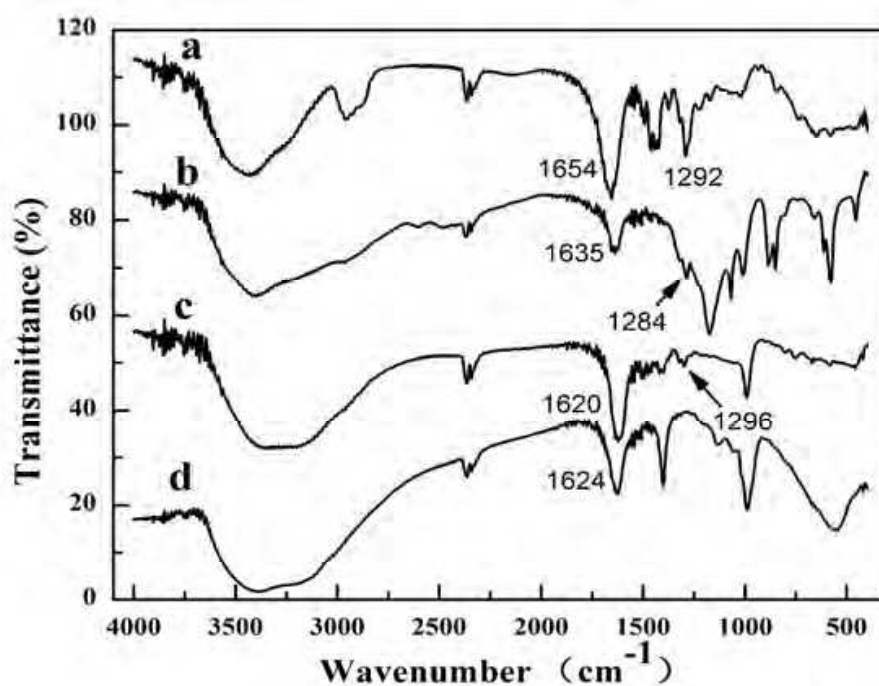Fig. 1. Polymer-assisted deposition process for VO$_2$ films.

Fig. 2. FTIR spectra of PVP (a), PVP with H$_2$SO$_4$ (b), precursor solution with PVP (c) and PVP-free vanadium solution (d). pH values of (b, c and d) were adjusted to the same.[43a]
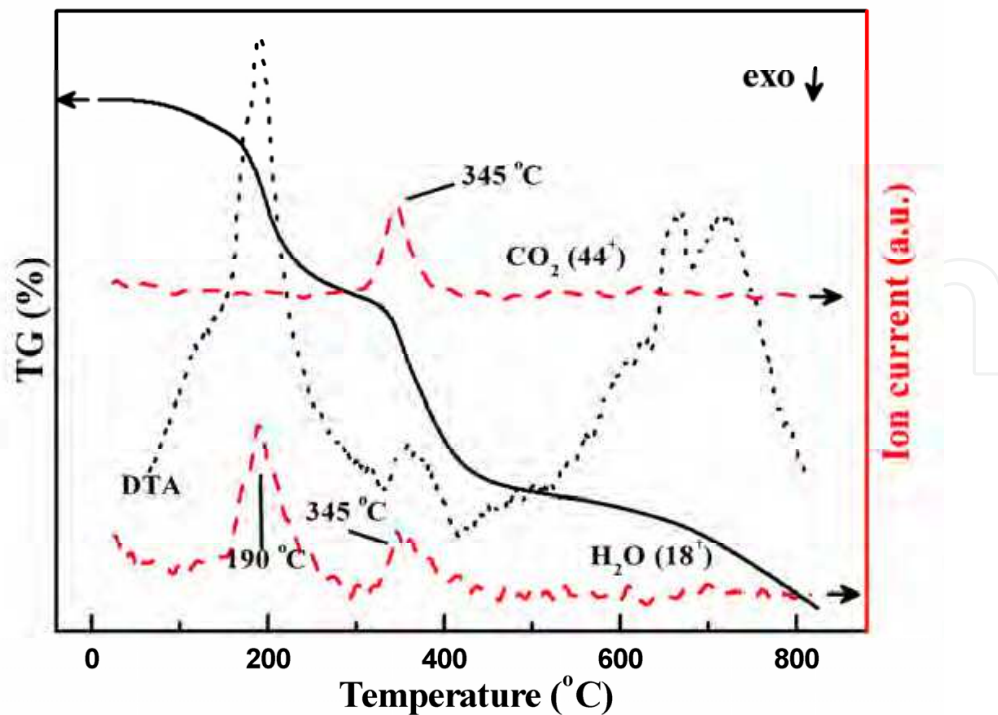
Fig. 3. Simultaneous TG, DTA and evolved gas analytical curves of 7.6 mg precursor gel containing K90 PVP with nitrogen flow of 30 mL·min^{-1}, heating rate of 10 °C·min^{-1} in an open Al$_2$O$_3$ crucible.[43b]
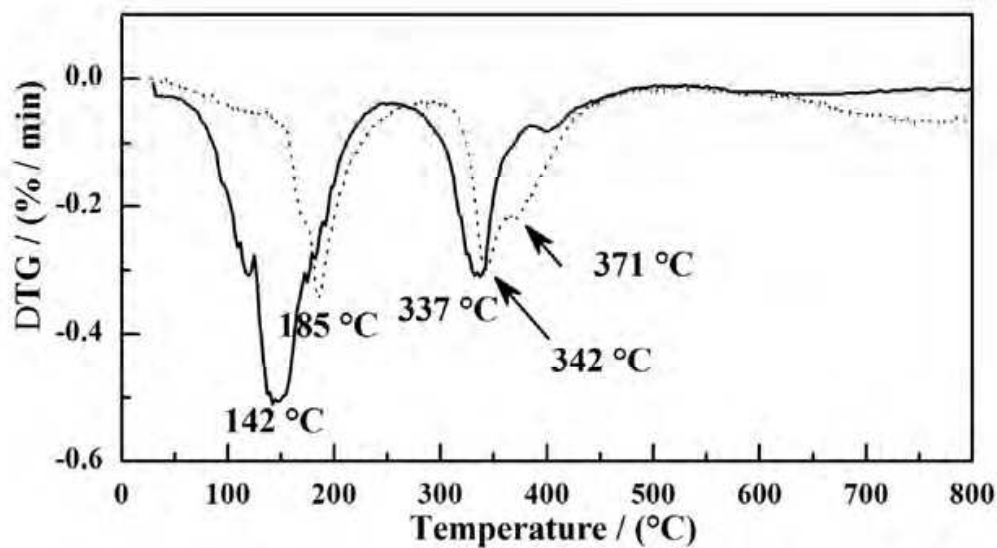

Fig. 4. DTG curves of precursor gel containing K90 (the dot line) and K30 PVP (the solid line) with nitrogen flow of 30 mL·min^{-1}, heating rate of 10 °C·min^{-1} in open Al$_2$O$_3$ crucibles.[43b]

The simultaneous TG, DTA, DTG and evolved gas analytical curves of the gel contain K90 PVP in a nitrogen atmosphere are presented in **Figure** 3 and **Figure** 4 (the dot line). On the basis of MS (mass spectrum) signals, the evolution of H$_2$O and CO$_2$ was detected (**Figure** 3).

At temperatures up to 250 °C, adsorbed and chemisorbed H_2O was released, indicating by MS and DTG changes centered at 185 - 190 °C (a continuous weight loss from 100 to 250 °C in TG) along with an endothermic peak in DTA. After the evaporation of water, there is a plat stage in both MS and TG curves from 250 to 300 °C.

At 300 - 450 °C, both H_2O and CO_2 were released, as observed distinct peaks in MS curves at 345 °C, implying the oxidization of PVP with a trace amount of oxygen in the nitrogen flow. CO is formed when oxygen is insufficient, although the MS signals for CO were failed to be detected due to the similar molecular weight of CO and N_2. This conclusion also can be drawn from the DTA/DTG results, in which an endothermic peak appeared at 360°C in the DTA curve (a corresponding shoulder at 371°C in the DTG curve). In the range of 450 - 650 °C, no obvious reactions occurred. Above 650 °C, a gradual weight loss in the TG curve was observed, implying that the residual carbon (which had been confirmed by Raman analysis) can further reduce VO_2 to V_2O_3 (from XRD results).

Further DTG analysis on precursor gels containing PVP of different molecular weights reveals that the decomposition sequence is related to the molecular weight of the polymer. As show in Figure 4, both DTG peaks for water desorption and polymer decomposition shifted to lower temperatures for the low molecular weight PVP (K30 vs K90). However, in both cases, heating temperatures ≥ 450 °C are needed to decompose the polymer. Therefore, the thermal analyses suggest that the appropriate annealing temperature for crystallization to thermochromic VO_2 should be in the range of 450 - 650 °C.
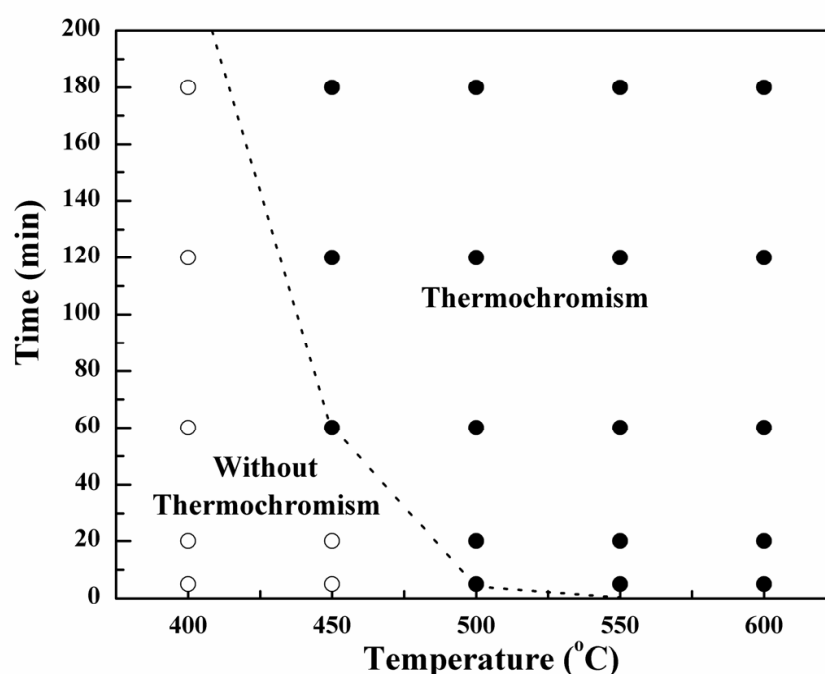
Fig. 5. Dependence of thermochromic properties on annealing parameters for VO_2 films from K30 PVP by annealing at a heating rate of 10 °C·min⁻¹ in N_2.[43b]

Subsequently, a series of annealing experiments were performed and the results are summarized in **Figure** 5. It was shown that at 450 °C a relatively longer annealing time was

required to crystallize VO$_2$ with thermochromic properties. At 500 °C and above, the annealing time could be significantly shortened, and holding time was even unnecessary. These results are coincident with those of thermal analyses, and are very profitable for scale-up mass manufacturing.

Interestingly, when K30 PVP was replaced by K90 PVP, the annealing time at 500 °C should be prolonged to exceeding 20 min to achieve the thermochromic properties. This result shows that the degradation process of polymers effectively influences the formation of thermochromic VO$_2$, probably due to interactions between PVP and VO^{2+} at the atomic scale. This conclusion supports the film-forming mechanism that we proposed in the previous work.[43a] Furthermore, these interactions ensure the formation of homogeneous hybrid precursor films after solvent evaporation.[43] Thereby, the morphologies of final films could be easily controlled via adjusting the degradation rate of polymers.

Figure 6 (a) shows the TEM image for precursor gel. PVP aggregates, inorganic clusters and their aggregates were clearly identified. Using this precursor solution, a homogeneous film was obtained, as show in **Figure** 6 (b). After crystallization, both PVP-free and PVP-employing films were particulate, porous, while the particle size of PVP-employing films (~100 nm in diameter) was much smaller than PVP-free ones (over ~100 nm) that showed a broad size distribution. The porosity of PVP-free films was obviously larger than PVP-employing films, typically about 63.5 % (**Figure** 7a and b) vs 17 % (**Figure** 7c and d) when it was analyzed by the software image-pro plus 5.0.
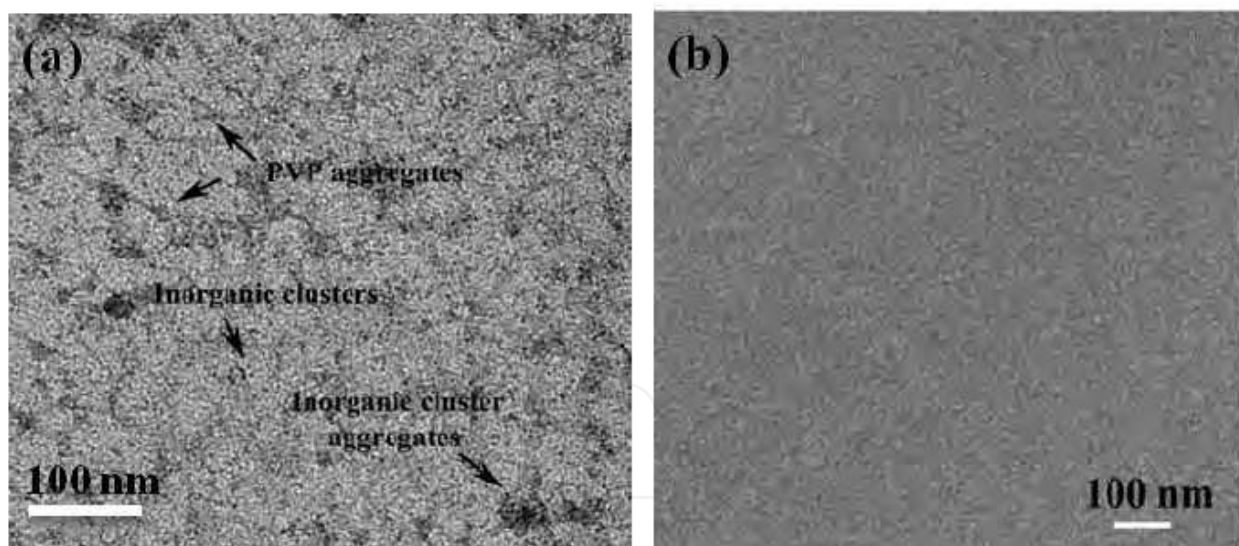

Fig. 6. (a) TEM images of precursor gel and (b) SEM image of precursor gel film.[43a]

A schematic illustration of film-forming mechanism was given in **Figure** 8. The interactions among polymer molecules via the oppositely charged groups along with that between the carbonyl groups and the metal ions ensured the formation of cross-linked high-quality gel films after the solvent evaporation. In addition, steric entangling of the polymer chains assists in the enhancement of cross linking.
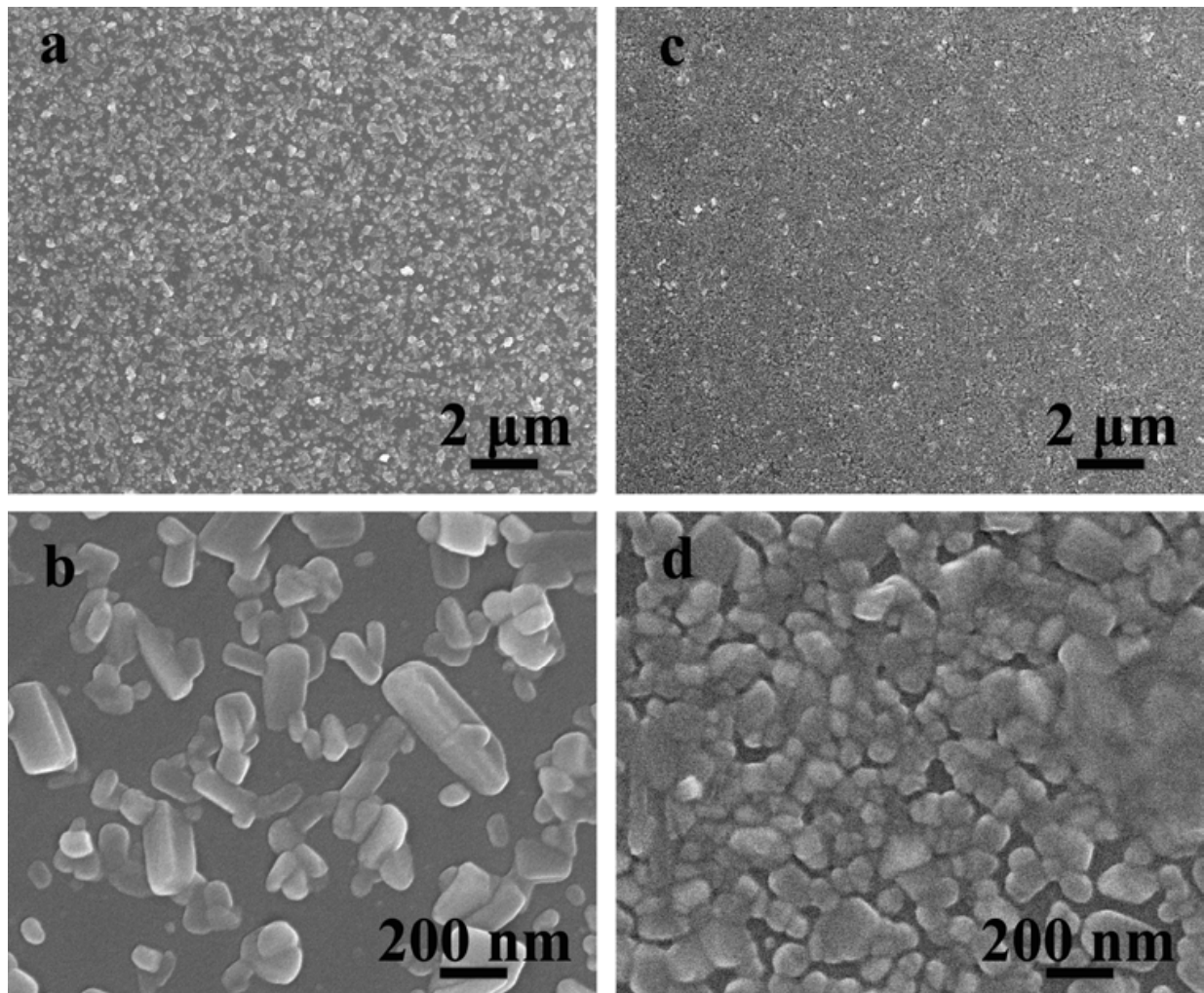
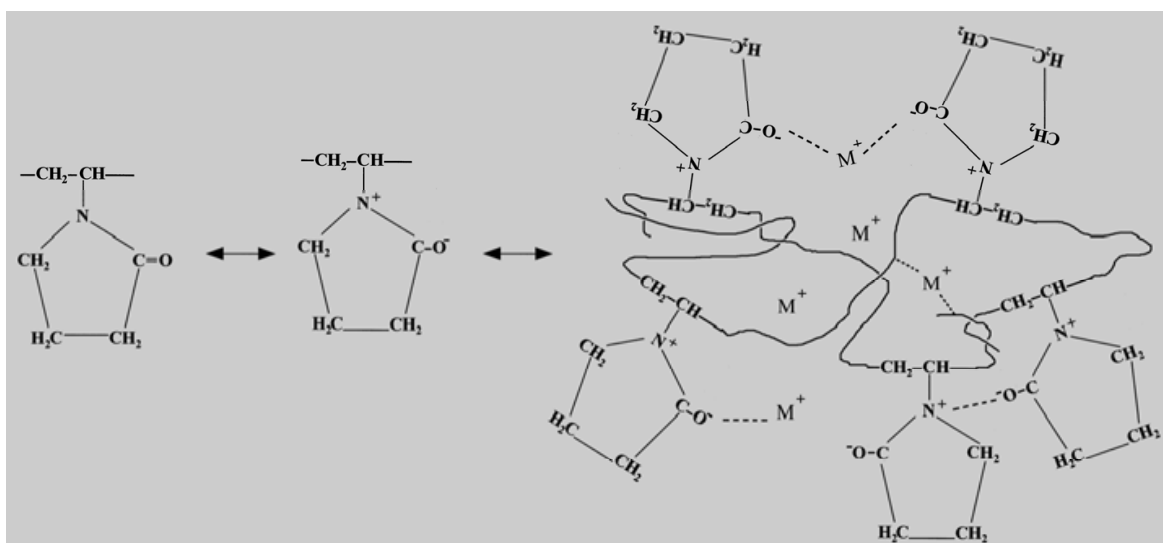Fig. 7. SEM images of a PVP-free film (a and b) and a PVP-employing film (c and d) on fused silica substrates.[43a]

Fig. 8. A schematic illustration of the interactions between aqua vanadium ions (M⁺) and PVP as well as the formation mechanism of precursor films.[43a]

2.2 The fundamental properties of single-layered VO₂ films

Figure 9 shows that the VO₂ film prepared by polymer-assisted deposition process had a relatively pure crystalline phase. For the film obtained by a PVP-free solution, only limited peak were detected, which were assigned to the characteristic peak of M-phase VO₂ (JCPDS Card No. 72-0514, P21/c, a = 0.5743 nm, b = 0.4517 nm, c = 0.5375, β = 122.61°), but two weak diffraction peaks at 9.36 ° and 12.24° were also detected, which were too skimpy to be determinately identified. For the film prepared by the PAD process, only M-phase VO₂ characteristic peaks (011) was detected, which suggested that the film was in a preferential orientation.

The formation of M-phase VO₂ was further confirmed by Raman spectra. At an output power of 1 mW (Figure 10, curve a) for a pure film, an almost complete set of Raman bands of M-phase VO₂ were observed. The bands agree well with references[9, 79-80] for M phase VO₂, with centers at 192, 222, 261, 308, 337, 391, 440, 497 and 615 and 816 cm⁻¹. There is at least one corresponding band for every Raman band of our film and the positions of the bands are agreed well with each other, meaning that every Raman bands we collected here can be assigned to M-phase VO₂. A Raman spectrum for a 1 at % W-doped VO₂ film (Figure 10, curve b) at 1 mW showed only weak bands, suggesting that the film was at the phase transition point due to the reduction effect of the W-doping on the transition temperature. No Raman bands appeared at output power of 20 mW for both of the films (Figure 10, curves c and d), indicating that complete phase transition from M-phase VO₂ to R-phase VO₂ occurred under this output power condition. The contribution of a fused quartz substrate has also been included (**Figure** 10, curve e) for the sake of comparison. Although an overlap of Raman bands of fused quartz and WO₃ at 807 cm⁻¹ makes it difficult to determine the presence of WO₃ from the enlarged Raman spectra of W-doped films, other strong Raman bands located at 716, 275 cm⁻¹ were not observed, excluding the absence of WO₃. Meanwhile, no obvious Raman bands for impure phases were found after the phase transition, indicating that there were no obvious impure vanadium oxides.
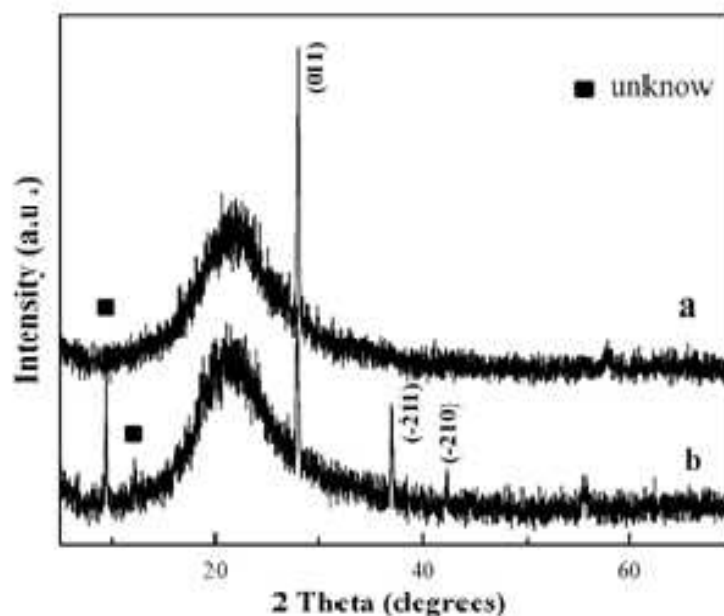

Fig. 9. XRD patterns of VO₂ film prepared by using a PVP-employing aqueous solution (a) and a PVP-free solution (b) on fused silica substrates.[43a]
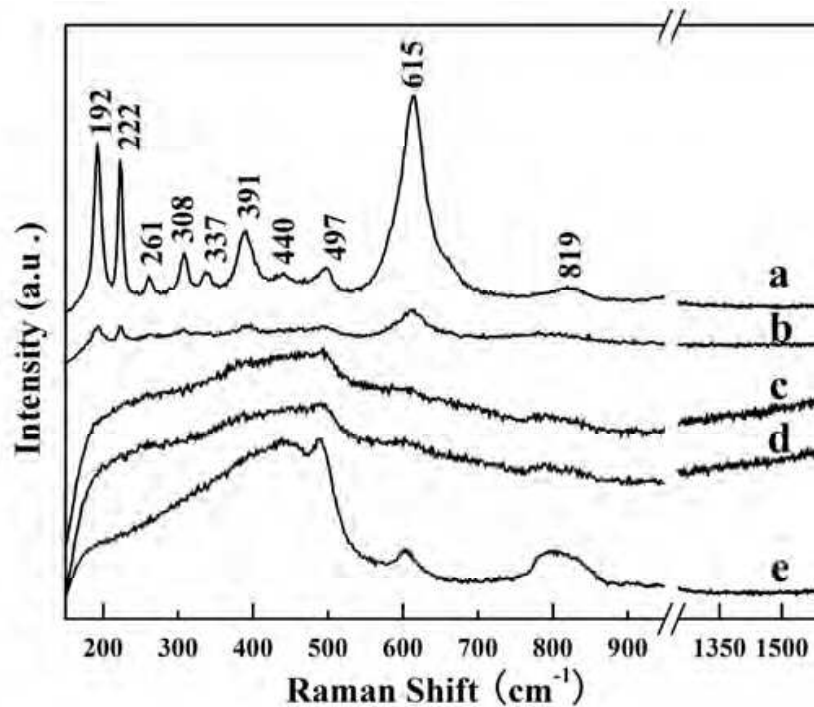
Fig. 10. Output power-dependent Raman spectra for PVP-employing VO$_2$ films on fused silica substrates (a-d) and a substrate only (e). (a) 1 mW (b) 1 mW and 1 at % W-doped film (c, e) 20 mW (d) 20 mW and 1 at % W-doped film. [43a]
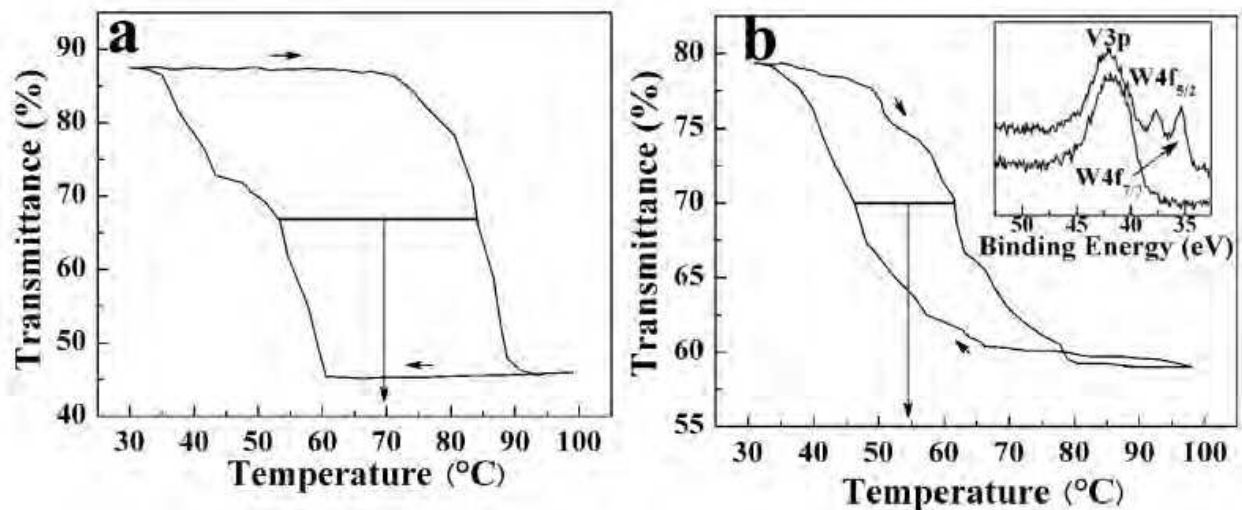

Fig. 11. Temperature dependence of optical transmittance at a fixed wavelength (2000 nm) for a pure (a) and a 1 at % W-doped (b) PVP-employing VO$_2$ film. The inset shows the W4f$_{5/2}$ and W4f$_{5/2}$ spectra for a pure (bottom) and a 1 at % W-doped (top) VO$_2$ film.[43a]

The 1 at % W-doped VO$_2$ film exhibits a hysteresis loop centered at 54 °C with a width of 16 °C (**Figure** 11b), implying a decrease in phase transition temperature of about 15 °C. This decreasing efficiency is less than other reports.[36,38] Significantly, the decreasing efficiency of phase transition temperature for 1 at % W-doped film was lower than the average efficiencies of other doping doses in references, which employed similar doping process to

prepare VO$_2$ particles,[81] probably because the tungsten ion was not completely incorporated into the final VO$_2$ films. W4f$_{5/2}$ and W4f$_{7/2}$ XPS peaks with a binding energy of 37.7 and 35.3 eV, respectively, are clearly seen in Figure 11b inset for the W-doped thin films and the tungsten ion in these films is W^{6+} according to the standard binding energy. The width narrowing of the hysteresis loop can be explained by the martensitic transformation model for VO$_2$.[82] W-doping increases the density of structural defects, which is a power function of the driving force, and relatively reduces the activation energy of the coordinated jumps of V cations (phase transitions take place at a certain defect density for size-fixed crystal grains[58]). Activation energy further influences the widths of hysteresis loops via degrees of supercooling or superheating. This deduction of martensitic transformation model is in agreement with various experiment results.[25,39,83]

2.3 Optimized thermochromic hysteresis properties of single-layered films

Thermochromic properties are important parameters for the practical application of this material. These parameters include phase transition temperature, thermochromic hysteresis and energy-saving efficiency. **Figure** 12 shows a schematic description of phase transition temperature and thermochromic hysteresis. From the transmittance (Tr) - temperature (T) data, a plot of d(Tr)/d(T) - T is obtained, yielding one or two peaks with well-defined maxima (see Figure 12). Each of the d(Tr)/d(T) - T curves has been fitted with a Gaussian function using the peak fitting module of *Originpro 7.5 software*. The temperature corresponding to the maximum d(Tr)/d(T) is defined as the phase transition temperature (T_c) of the branch ($T_{c,h}$ and $T_{c,c}$ represent T_c of heating and cooling branches, respectively). For cooling branches, the appearance of steps introduces two peaks in the d(Tr)/d(T) - T
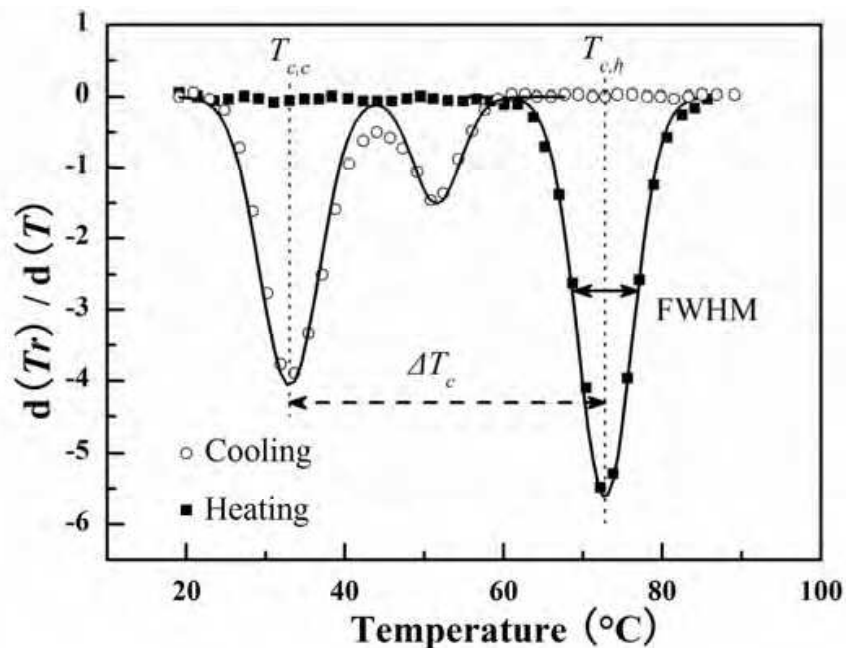

Fig. 12. A schematic description of the definition of the S-M transition parameters for heating and cooling branches using the d(Tr)/d(T) - T plot. T and Tr represent temperature and transmittance at wavelength of 2000 nm. The resulting parameters $T_{c,h}$, $T_{c,c}$, ΔT_c and FWHM of peaks are employed to express phase transition temperature of heating, cooling branches, the width of the hysteresis loop, and the slope of the transition, respectively.[44]

curves. The T_c values of these branches are determined by the main peaks. The slope of the transition is expressed by the full width at half maximum (FWHM) of the peak. The width of the hysteresis loop, ΔT_c, is defined as the temperature difference of $T_{c,h}$ - $T_{c,c}$.

Figure 13 shows typical SEM photos of VO$_2$ films heated at 600 °C for different times with a heating rate of 30 °C·min^{-1}. All the films are porous, consisting of irregular particles. The pore formation is attributed to the degradation of PVP and the shrinkage of the gel film during annealing. Grain boundaries change from clear (**Figure** 13a, b, c) to fuzzy (inset in **Figure** 13d) as the annealing time is prolonged. Meanwhile, the particle size varies dramatically, associated with distinct change of porosity and pore shape. To evaluate the differences of particle size among samples, the distributions of particle sizes was measured. The corresponding size distribution scatter graph as well as fitting curves with Gaussian distribution is shown in **Figure** 14. The scatter graphs were plotted by randomly measuring the dimensions of 300 grains in a given micrograph. The particle size distribution scatter graphs of **Figure** 13d failed to be obtained due to fuzzy grain boundaries. The results showed that the grain size of Sample I complied with Gaussian distribution, while the
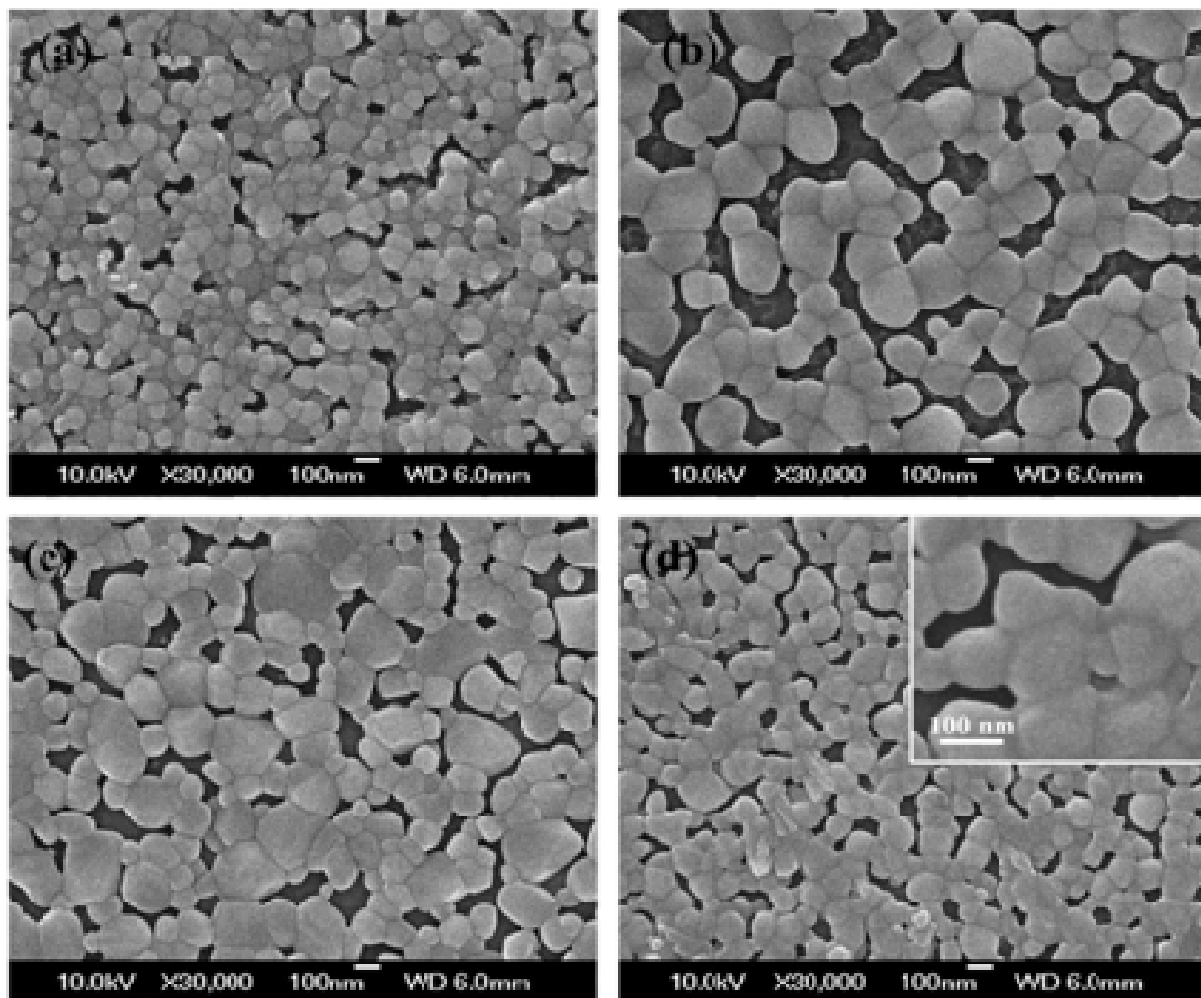

Fig. 13. SEM photos of Sample I (a), Sample II (b), Sample III (c) and Sample IV (d). Samples were obtained by annealing at 600 °C for different times, 5 min (a), 20 min (b), 60 min (c) and 180 min (d) with heating rate of 30 °C·min^{-1}. The inset of photo (d) is a high resolution SEM photo of sample IV. [44]

distributions for Samples II and III distinctly exhibited two maxima. The size distribution scatter graphs indicated that when annealing time increases from 5 to 20 min, the particle size increases rapidly (**Figure** 13a, b and **Figure** 14a, b). However, the VO₂ particles shrink noticeably for the long time annealing samples (**Figure** 13c and **Figure** 14c, d), resulting in few large particles and a broad distribution of particle sizes. The shrinkage of particle size (which is also observed in the 500 °C annealed films) and change of grain boundaries are tentatively attributed to the mass transport via surface diffusion during annealing. This mass transport has been reported as the main reason for morphology evolution of VO₂ films during the heat treatment of pre-deposited amorphous ones at 450 °C.[83]
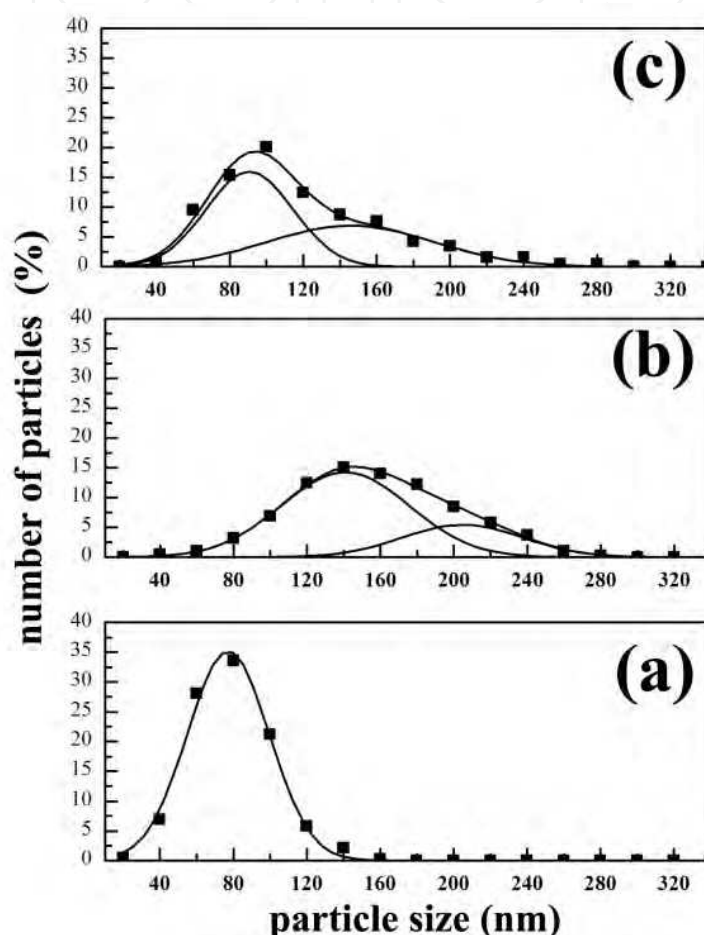

Fig. 14. Scatter graphs showing the particle size distributions in Sample I (a), Sample II (b) and Sample III (c). The solid curves are those after fitting by Gaussian distribution. Samples were obtained by annealing at 600 °C for different times, 5 min (a), 20 min (b) and 60 min (c) with heating rate of 30 °C·min⁻¹.[44]

Significantly, obvious steps were observed at the cooling branches for Samples I, II and III (insets of **Figure** 15a, b, c, annealing for 5, 20 and 60 min, respectively). The appearance of steps suggests another loop width. The steps are resulted from a difference in temperature of inhomogeneous occurrence of phase transition in the films due to the two-humped grain size distributions (**Figure** 14b, c)[84] or the site-selective nucleation of product phase, as observed in literature.[85] However, there are also some contradictions. First, this deduction is difficult to explain the step appearing in Sample I, which manifests a Gaussian distribution

with one maximum in grain size. Second, this deduction suggests that the temperatures of the $d(Tr)/d(T)$ - T peaks should vary as the size distribution changes. For Sample II and III, however, although the size distribution curves are quite different (**Figure** 14b, c), the step appears at similar temperatures on the cooling branch of the $d(Tr)/d(T)$ - T curves. Therefore, it seems that these experiment results don't agree to the model suggested by Klimov, V. A et al..[84] In fact, the propagation of the phase transition through grain boundaries may possibly counteract inhomogeneous distribution of T_c in the VO_2 films. Therefore, there is usually no step observed in relatively narrow hysteresis loops.[86-87] It is believed that any models related to the steps in the hysteresis loops should take the influence of grain boundary into account.
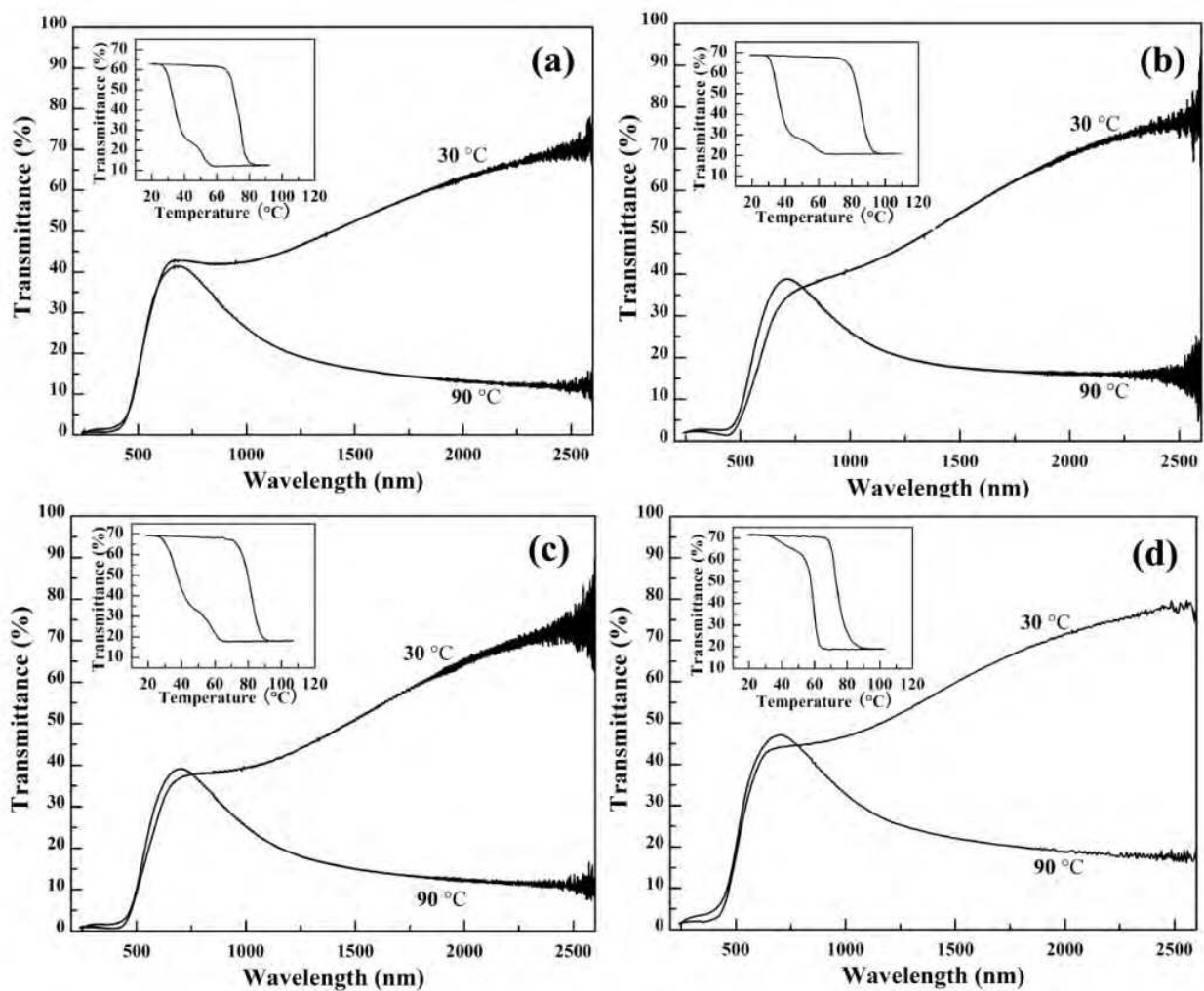

Fig. 15. Optical transmittance spectra and temperature dependence of optical transmittance (insets) at a fixed wavelength (2000 nm) for Sample I (a), Sample II (b), Sample III (c) and Sample IV (d). Samples were obtained by annealing at 600 °C for different times, 5 min (a), 20 min (b), 60 min (c) and 180 min (d) with heating rate of 30 °C·min^{-1}. [44]

For Sample IV (annealed for 180 min), the step seems to be depressed (inset of **Figure** 15d). This result could be explained by the coalescence of grain boundaries and the improvement of phase transition propagation through grain boundaries, which would push the step upward. The appearance of the step in only one of the two branches is associated with the asymmetry of the elementary hysteresis loops (i.e., the loops assigned to individual grains) with respect to the phase equilibrium temperature.[86] The asymmetry of the elementary hysteresis loops, in turn, is attributed to a transition temperature shift accompanying with a decrease in grain size,[88-89] or with stress at the substrate/film interface.[86, 90]

To further clarify the effects of grain size on the widths of hysteresis loops, films with similar morphologies and relatively homogeneous size distribution are needed. The current solution process enables us to achieve widely morphology control. In previous research, we have revealed that the precursor solution is in a state of solution rather than sol. After the solvent evaporation, the interactions among polymer molecules, along with those between the carbonyl groups and the metal ions, ensure the formation of cross-linked high quality gel films.[43a] In these films, the metal ions are bonded with the polymer through electrostatic interactions, forming a uniform organic-inorganic hybrid precursor film. The formation of metal oxide occurs after degradation of polymer begins.[43, 91] Therefore, the morphologies of final films could be easily controlled via adjusting the degradation rate of polymers. Meanwhile, for crystallization in a solid-state reaction, the dependence of nucleation and growth rate on temperature is usually different.[92] Thus, it is expected that the morphologies of VO$_2$ films could be tailored by variations of heat treatments. Accordingly, the films have been prepared under the same synthesis conditions as Samples I - IV, but at an annealing temperature of 500 °C. And the typical SEM photos and optical transmittance spectra, along with the hysteresis loops, are shown in Figure 16.

The sample obtained by annealing at 500 °C for 5 min showed a bluish color, but almost no thermochromic properties, and is excluded. Films produced at this annealing temperature have similar morphologies (Figure 16a, b, c). Compared to films obtained by annealing at 600 °C, in which many quasi-isolated grains appear, all of these films show grains tightly connected across boundaries. The grain sizes are smaller than those treated at 600 °C. The film obtained by annealing for 20 min (Sample V) consists of connected, irregular particles (Figure 16a). Typically, the largest dimension of each particle is around 100 nm. These particles possess flat surfaces, indicating that the mass transport during annealing is feeble for a short annealing time. The film produced by annealing for 60 min (Sample VI) shows similar granular morphologies with a relatively large roughness, and the particle size is reduced notably (Figure 16b). Prolonging the annealing time to 180 min (Sample VII) results in increases in porosity and surface roughness (Figure 16c), indicating the enhancement in mass transport that changes the surface morphology of these particles.[83, 92]

To further verify our discussion on grain boundaries, two films (Sample I and Sample VIII) were scraped off from their substrates and observed by TEM (Fi**gure** 17). **Figure** 17a, b and c present TEM photos of Sample I. It is shown that the sample is assembled from irregular particles. Distinct grain boundaries are observed in high resolution TEM photos (**Figure** 17a, b and c), indicating that the grain boundaries are very loose in this film. The Fourier transform (FFT) patterns of corresponding crystal grains (**Figure** 17 insets) reveal diffraction spots, verifying the crystallinity. Significantly, the diffraction spots in the FFT patterns become hazy or disordered in the vicinity of grain boundaries. This experimental phenomenon can be ascribed to the poor crystallization of VO$_2$ under short annealing time
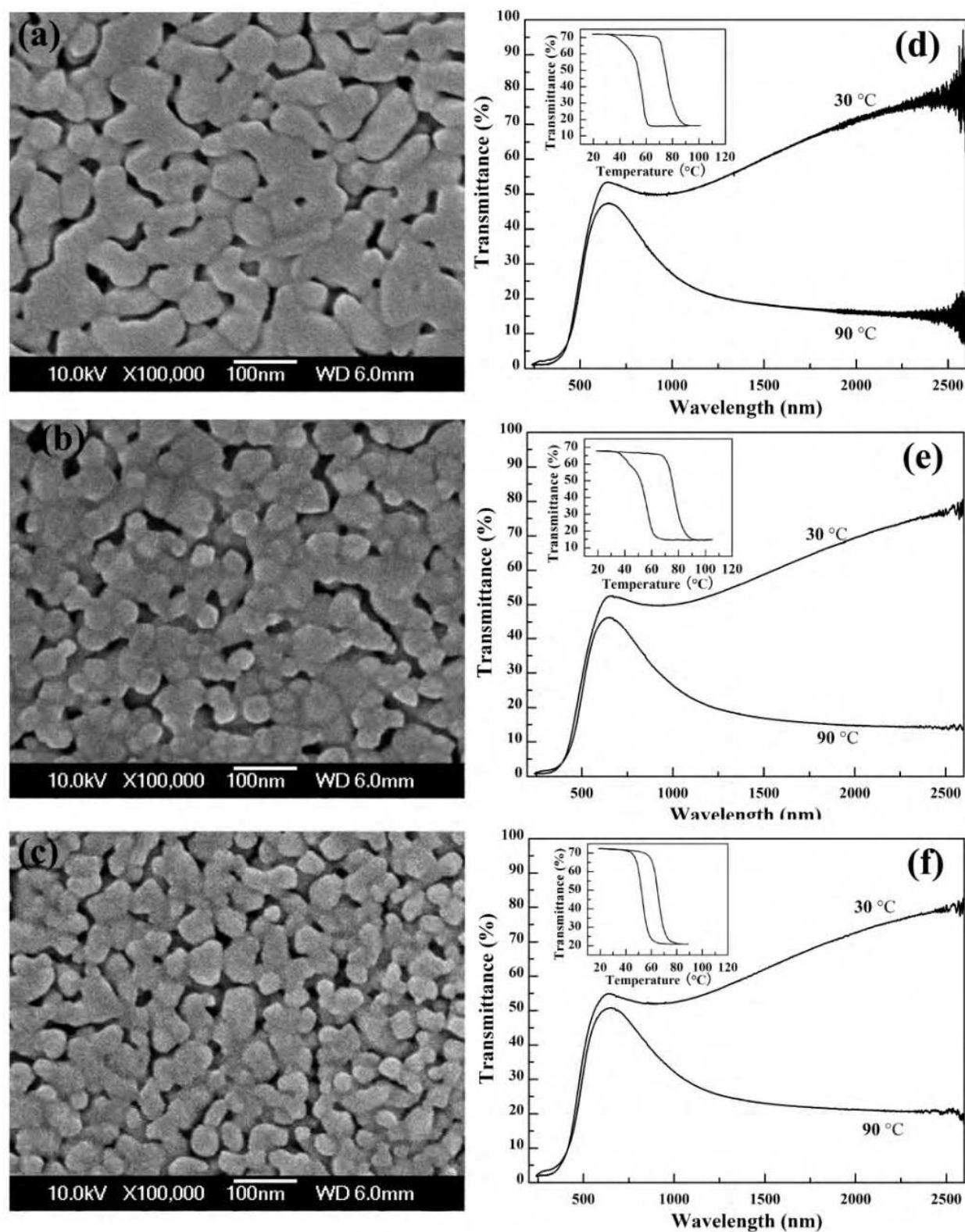
Fig. 16. SEM photos and optical transmittance spectra of Samples V (a and d), VI (b and e) and VII (c and f). Insets show corresponding hysteresis loops at 2000 nm. Samples were obtained by annealing at 500 °C for different times, 20 min (a and d), 60 min (b and e) and 180 min (c and f). Heating rate is the same, 30 °C·min⁻¹. [44]

(600 °C, 5 min). Generally, spaces about 2-5 nm in width were observed between grains, and they were attributed to poorly crystallized phases and/or voids. It is widely reported that VO$_2$ films with second or amorphous phases at grain boundaries demonstrate a broadened hysteresis,[82, 93, 94] which is definitely consistent with our experiments.

Sample VIII, on the other hand, consisted of smooth connected particles and interconnected pores among particles (**Figure** 17d, e). This morphology should be a result of mass transport and aggregation of the primary VO$_2$ crystals during annealing.[83] The high magnification TEM photo clearly demonstrates that the grain boundaries are very sharp (**Figure** 17f). In fact, it seems that the lattice fringes pass through grain boundaries. The FFT patterns (**Figure** 17f insets) of the corresponding crystal grains are composed of two groups of bright diffraction spots, confirming the existence of boundaries and the high crystallinity of these crystals. The TEM photos are fully consistent with the SEM results (**Figure** 13a and **Figure** 16a) and the deductions from optical measurements (**Figure** 15a inset and **Figure** 16b inset).
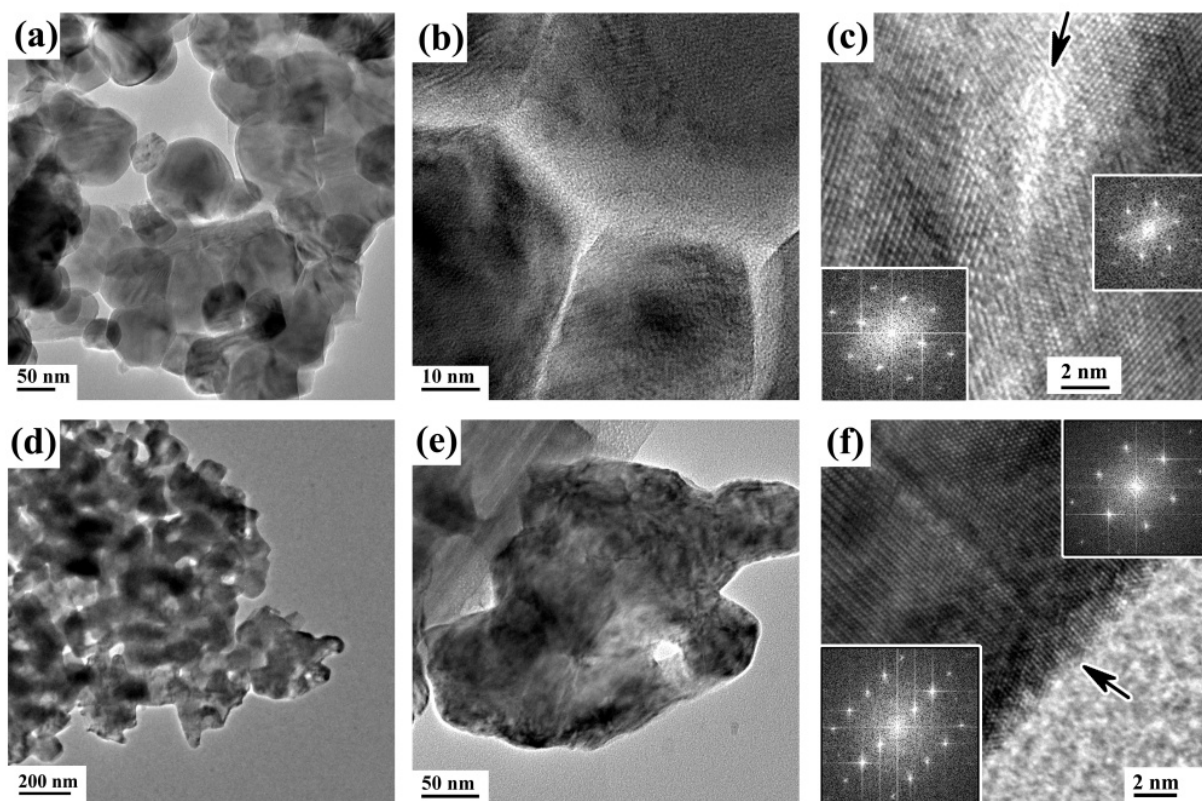

Fig. 17. TEM photos of Sample I (a, b and c) and Sample VIII (d, e and f). The insets of photos c and f are FFT patterns of corresponding crystal grains. Samples were obtained by annealing at 600 °C for 5 min (a, b and c) with a heating rate of 30 °C·min^{-1}, and 500 °C for 180 min (d, e and f) with a heating rate of 3 °C·min^{-1}, respectively. [44]

To evaluate the optical and thermochromic properties of the samples, the integral transmittances of films annealed with heating rate of 30 °C·min^{-1} were calculated in the visible region (380 - 780 nm), so were the integral infrared transmittance reductions before and after the S-M phase transition in the wavelength of 1500 - 2500 nm. The results are shown in **Figure** 18. According to the theory suggested by J. Narayan and V. M. Bhosle,[57] the amplitude of the transition should deteriorate as the defect content increases. It is expected

that the 500 °C annealed samples should be less crystallized and thus contain high defect content. Accordingly, they should exhibit deteriorated infrared transmittance reduction compared with the 600 °C annealed samples. This phenomenon was not obviously detected in our films, even though the hysteresis widths of the films vary considerably. In fact, it is clearly revealed that the 500 °C annealed samples show better visible transmittance than those annealed at 600 °C, while the infrared transmittance reduction remains comparable. For instance, the infrared transmittance reduction of sample VI (53.8%, 500 °C, 60 min annealed sample) is a little larger than that of sample II (51.2%, 600 °C, 20 min annealed sample). Meanwhile, the integral visible transmittance of sample VI (34.5%) is much higher than that of sample II (20.2%).

The difference in the microstructure and crystallinity had effects on the optical properties of these films. Hemispherical reflectance spectra of Sample II and VI were collected from 240 to 2600 nm (**Figure** 19). It was found that the integral hemispherical reflectance of Sample VI (18.7%) was 3.5% larger than that of Sample II (15.2%) in the visible region. Because both of the integral transmittance and integral reflectance for Sample II are smaller than those of Sample VI in the visible region, one can conclude that the absorption and/or scattering of Sample II are much larger. The hemispherical transmittance of the sample was recorded, in order to eliminating the influence of scattering. It was still shown that both the hemispherical transmittance and the hemispherical reflectance of Sample II are less than those of Sample VI in the visible region, indicating that the absorption of Sample II is larger than that of Sample VI.
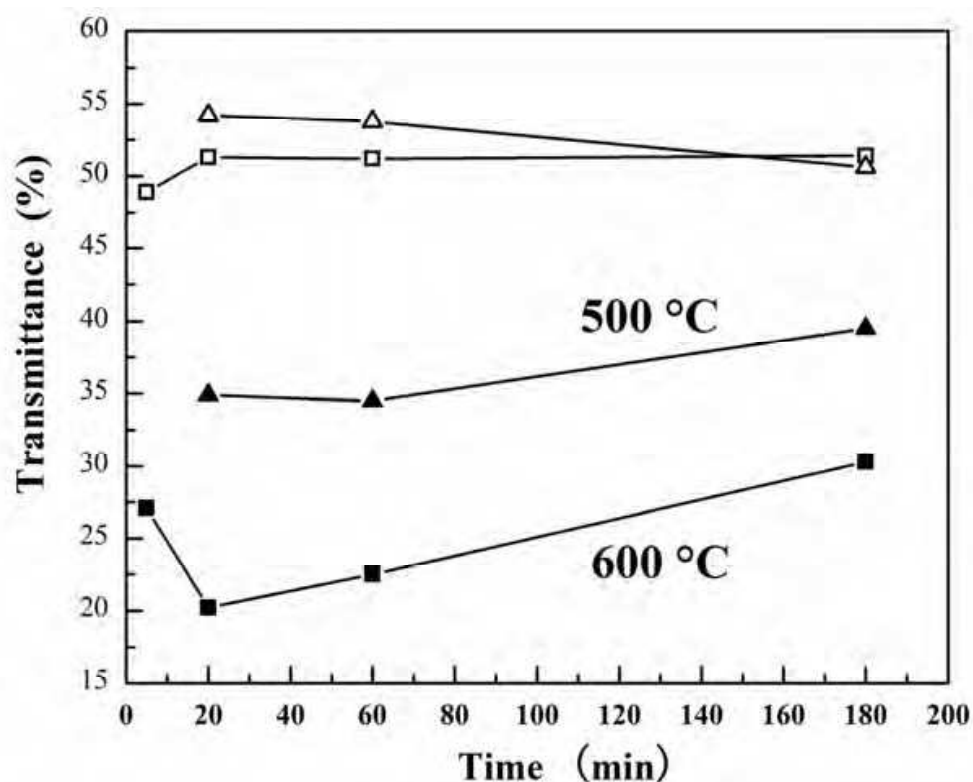

Fig. 18. Integral visible transmittance (in a region of 380 - 780 nm, filled polygons) and integral infrared transmittance reduction (in a region of 1500 - 2500 nm, open polygons) of films annealed at 600 °C (squares, Samples I - IV) and 500 °C (triangles, Samples V - VII) with heating rate of 30 °C·min^{-1}. [44]
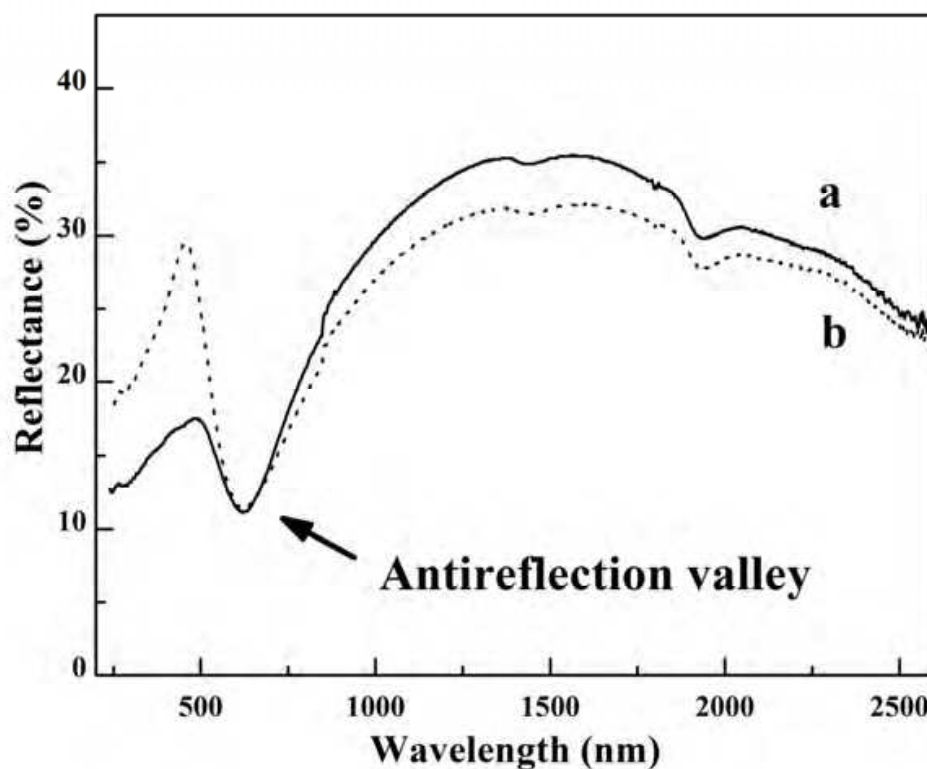
Fig. 19. Reflectance spectra of Sample II (a) and Sample VI (b). Samples were obtained by annealing at 600 °C for 20 min (a), 500 °C for 60 min (b) with heating rate of 30 °C·min⁻¹. [44]

2.4 Optimized visible transmittance of single-layered films

For the practical application of VO₂-based smart windows, a low luminous transmittance (T_{lum}) and solar modulating ability (ΔT_{sol}) are two major drawbacks. The T_{lum} and T_{sol} values were obtained from

$$T_{lum,sol}(\tau) = \int \varphi_{lum,sol}(\lambda)T(\lambda,\tau)d\lambda \,/ \int \varphi_{lum,sol}(\lambda)d\lambda \,,$$

where φ_{lum} is the spectral sensitivity of the light-adapted eye and φ_{sol} is the solar irradiance spectrum for an air mass of 1.5 (corresponding to the sun standing 37° above the horizon). ΔT_{sol} is obtained from

$$\Delta T_{sol} = T_{sol,l} - T_{sol,h} \,,$$

where l and h denote low- and high-temperature, respectively.

Strategies to improve T_{lum} and ΔT_{sol} have been investigated, including Mg- or F-doping,[33, 95] multilayer-stack design,[35,96] and composite film construction.[97] Besides a depression in transition temperature, Mg- or F-doping causes a blueshift in the absorption edge of VO₂ films (from around 445 to 415 nm).[95] This change results in a significant increase of the luminous transmittance at the expense of infrared modulating ability (wavelength ≥ 1000 nm).[33] Similar trade-offs between the luminous transmittance and thermochromic properties have also been observed in VO₂-based multilayer films.[35] A VO₂-SiO₂ composite film shows a high visible transmittance but weak infrared regulation ability.[97] Five-layered TiO₂/VO₂/TiO₂/VO₂/TiO₂ films with optically optimized structures have a relatively

higher luminous transmittance and solar modulating ability.[98] However, incorporating dielectric layers with a certain refractive index and thickness into complicated stack structures is a difficult technological challenge. Optical calculations suggest that VO_2 nanoparticles distributed in a dielectric matrix have higher T_{lum} and ΔT_{sol} than pure VO_2 films.[99] This study further predicts that a limit for noticeable solar energy modulation is $T_{lum} = 40\%$, and $\Delta T_{sol} \leq 10\%$.[99] We have recently confirmed experimentally the effects of composite matrix.[68] VO_2-ZrV_2O_7 composite films with similar thickness of about 95 nm showed decreased particle sizes and significantly enhanced luminous transmittances (from 32.3% at Zr/V=0 to 53.4% at Zr/V=0.12) with increasing Zr/V rations.

However, the influence of porosity on optical properties of single-layered VO_2 films, which should have priority over the stack structure of VO_2-based multilayers, is seldom reported. Pores with air in VO_2 films can be considered as a secondary component that should have similar effects on improving T_{lum} and ΔT_{sol}. In this study, calculations confirm that optical constants and film thickness have important effects on the thermochromic properties of these films. An optical-admittance recursive method was used to simulate the spectral transmittance using the optical constants of VO_2 and a fused-silica-glass substrate. The optical constant is assumed to be linearly dependent on the volume fraction.[100] **Figure** 20 shows the computed luminous transmittance and solar modulation of VO_2 films with different thicknesses and porosities. The results indicate that ΔT_{sol} could be increased without decreasing T_{lum} by increasing the porosity, which is derived from the depression of the reflection.
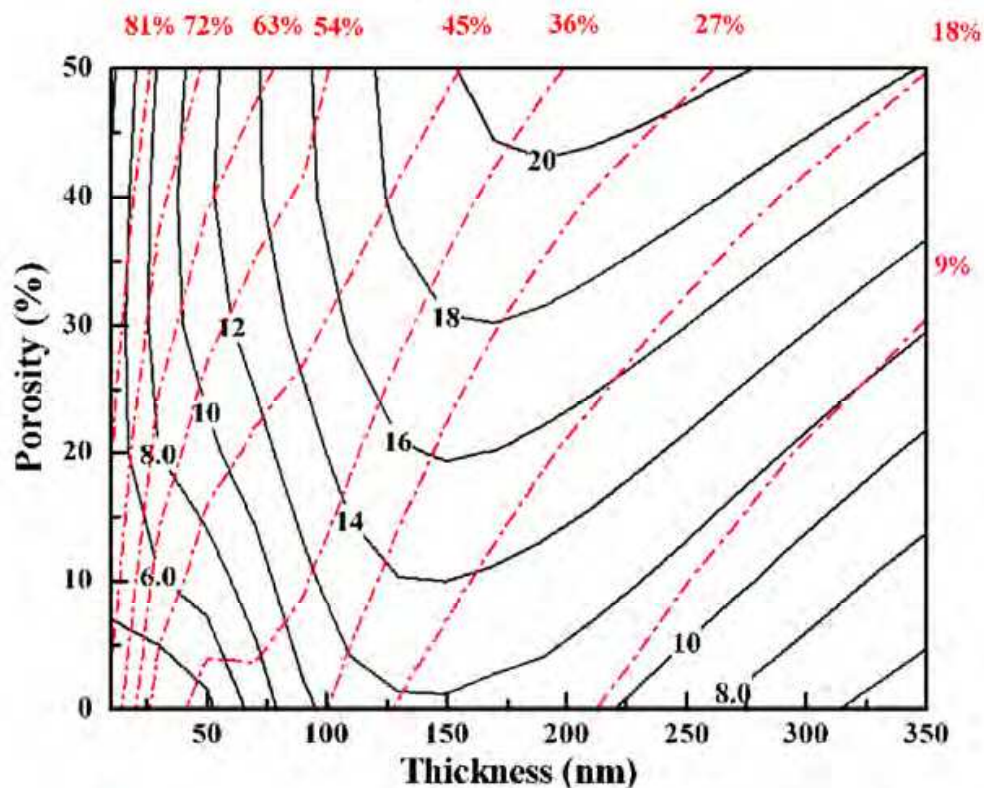

Fig. 20. Computed luminous transmittance in an insulator state ($T_{lum,I}$, red dot lines) and solar modulation between MIT (ΔT_{sol}, black solid lines) as a function of the thickness and porosity of the VO_2 films.[69]

To validate the above prediction, we prepared VO$_2$ films by PAD. X-ray diffraction and Raman spectra confirmed the formation of a monoclinic (M) phase with a trace amount of V$_2$O$_5$. **Figure** 21a shows a top-down SEM image of VO$_2$ films, which reveals that the sample consisted of interconnected VO$_2$ particles and irregular nano-pores. The size of particle and pore ranges from 20-70 and 15-80 nm with a mean value of 38 and 28 nm, respectively. The feature size of the film is well below the wavelength of visible and infrared light, favoring the improvement of optical quality. The nano-porous feature of the films is observable (inset of **Figure** 21a), which is also supported by the low *n* and *k* values of ellipsometry results compared with those in the literature (**Figure** 21b).[46] For example, the value of *n* is 2.2 for our VO$_2$ film, which is around 3 in the literature.[46] The result also shows that T_{lum} in the current research is much higher (by ≥12%) than that in the literature with comparable ΔT_{sol} due to the different optical constants (**Figure** 21b).[46] These results are attributed to the degradation of PVP and the shrinkage of the gel film during annealing.[43a]
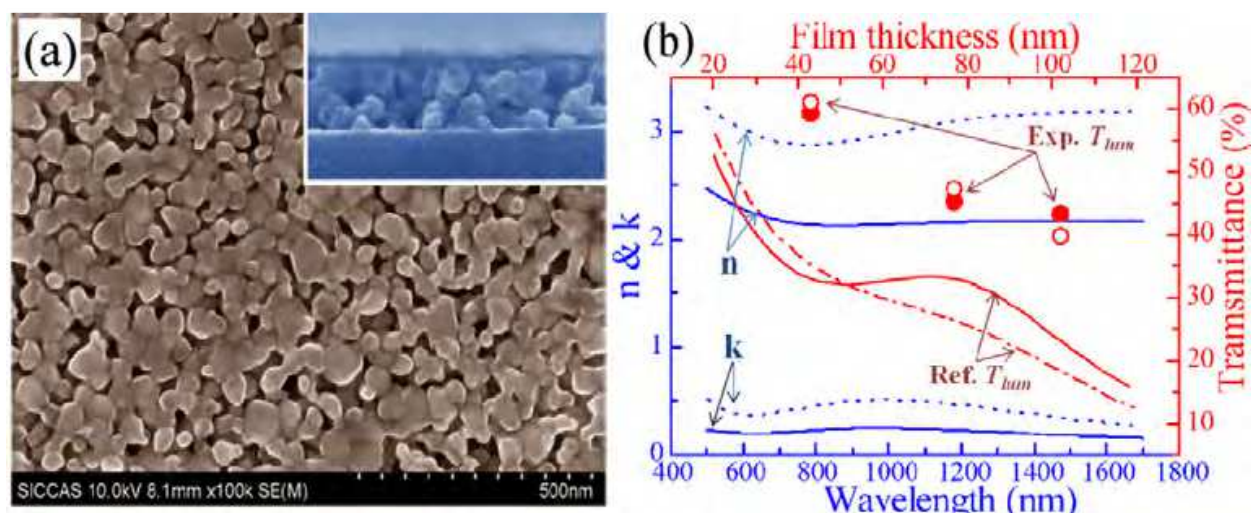

Fig. 21. Part (a) shows a SEM image of a 147-nm-thick VO$_2$ films on quartz glass. The inset of (a) is a cross-sectional SEM image. Part (b) shows the experimental (solid lines) and reference (dotted lines) optical constants at 20 °C as well as experimental (Exp. T_{lum}) and reference (Ref. T_{lum}) integral luminous transmittance of the film at 20 (solid symbols) and 90 °C (open symbols), respectively. The reference data are redrawn from Reference 46. [69]

Figure 22 shows the transmittance and reflectance spectra of typical VO$_2$ films. The MIT transition is clearly observed as a dramatic infrared-transmittance change with temperature (**Figure** 22a). T_{lum} reduces steadily with increasing film thickness, which is ascribed to the strong absorption of VO$_2$ in this region.[44, 99] The change in the infrared transmittance of VO$_2$ films at 90 °C with different film thicknesses shows a similar behavior. Nevertheless, the infrared transmittance at 20 °C for a 428-nm-thick film is obviously higher than that of a 215-nm-thick film after 1700 nm (**Figure** 22a). These changes in the transmittance spectra correspond to reflectance valleys in **Figure** 22b, suggesting the existence of a self-antireflection effect in these thicknesses due to the destructive interference of light reflected from the film-substrate and the air-film interfaces.
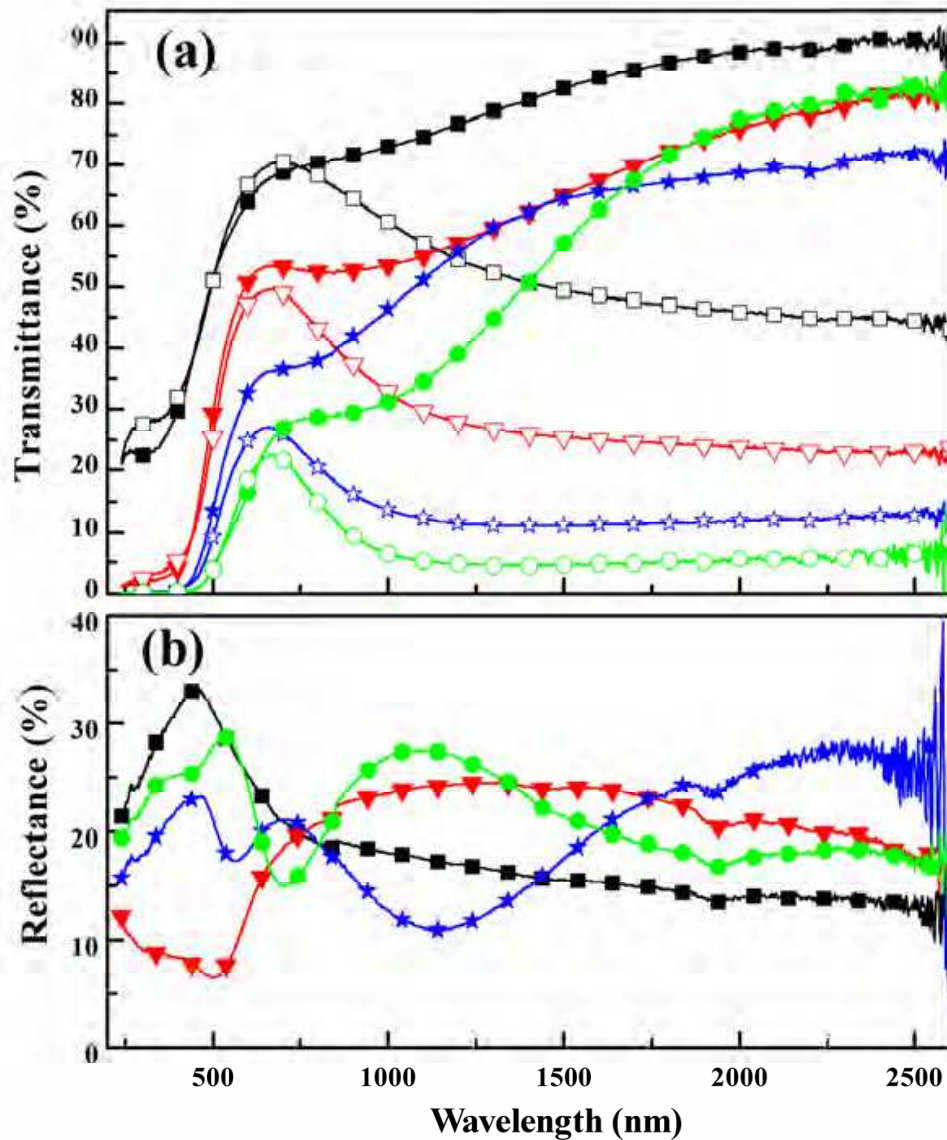
Fig. 22. Thickness dependence of transmittance (a) and reflectance (b) spectra for typical samples with different thicknesses (43, 102, 215 and 428 nm corresponding to the black squares, the red triangles, the blue pentagrams and the green circles, respectively). The transmittance was measured at both 20 °C (lines with solid symbols) and 90 °C (lines with open symbols) and the reflectance was measured at only 20 °C.[69]

The change of the optical constants of VO_2 across the MIT can effectively modulate the infrared transmittance and shift the position of the reflectance valley at 20 °C, leading to a significant enhancement of the IR modulating ability at a certain wavelength. This phenomenon could be harnessed to boost the thermochromic properties of a single-layer film in selected wavelength ranges. For instance, a 215-nm film shows a transmittance change of 50% (from 61.1% to 11.1%) at 1350 nm across the MIT, the highest value at this wavelength to our knowledge. Furthermore, the enhancement of the IR modulating ability could be adjusted to longer wavelengths by a simple regulation of the film thickness. A 428-nm-thick VO_2 film exhibits a IR transmittance change of 76.5% (from 83% to 6.5%) at 2500 nm, even prior to the optimized result of sputtering films (74%).[19]

Another interesting phenomenon is that the changes in luminous transmittance (ΔT_{lum}) across the MIT are thickness dependent. For thin films, the visible transmittance at 20 °C is generally lower than that at 90 °C (**Figure** 22 and Table 1) and, vice versa. The visible transmittance at 20 °C for the above 100-nm-thick films exceeds that at 90 °C (**Figure** 22b and Table 1). This reversion in ΔT_{lum} is ascribed to interference effects and was also reported by Xu et al.[46]

In view of the fact that solar energy is mainly in the visible region with a peak at 550 nm, the ΔT_{lum} reversion across the MIT effectively influences ΔT_{sol}. For instance, ΔT_{sol} increased by only 0.6% (from 6.4% to 7.0%) as the film thickness increased from 43 nm to 77 nm. Nevertheless, compared with the 77-nm-thick film, ΔT_{sol} largely increased from 7.0% to 14.1% for the 102-nm-thick film. Meanwhile, the $T_{lum,l}$ remained almost unchangeable (45.3% and 43.3% for the 77- and 102-nm-thick films, respectively). Further increasing the film thickness to 147 and 215 nm increased ΔT_{sol} gently to 16.6% and 18.6%, accompanied by an evident depression in T_{lum}. Both T_{lum} and ΔT_{sol} were reduced for the 428-nm-thick film. Therefore, the optimized thickness for films prepared by this system to balance T_{lum} and ΔT_{sol} is 100 nm. The single-layer film of this thickness shows comparable T_{lum} and ΔT_{sol} values to those of five-layered $TiO_2/VO_2/TiO_2/VO_2/TiO_2$ films with optically optimized structures ($T_{lum,l}$ = 45%, $T_{lum,h}$ = 42% and ΔT_{sol} = 12%, from $T_{sol,l}$ = 52% to $T_{sol,h}$ = 40%).[100]

Sample	Thickness (nm)	$T_{sol,l}$ (%)	$T_{sol,h}$ (%)	ΔT_{sol} (%)	$T_{lum,l}$ (%)	$T_{lum,h}$ (%)	ΔT_{lum} (%)
I	43	62.1	55.7	6.4	59.2	61.1	-1.9
II	77	48.1	41.1	7.0	45.3	47.2	-1.9
III	102	42.9	28.8	14.1	43.3	39.9	3.4
IV	147	39.4	22.8	16.6	33.7	29.4	4.3
V	215	32.9	14.3	18.6	28.7	19.2	9.5
VI	428	23.0	9.2	13.8	11.5	12.6	-1.1

Table 1. Optical properties of typical samples with different thicknesses; *l* and *h* mean low-temperature (20 °C) and high-temperature (90 °C), respectively.[69]

In summary, nanoporous thermochromic VO₂ films with low optical constants and tunable thicknesses have been prepared by polymer-assisted deposition. The film porosity and thickness change the interference relationship of light reflected from the film-substrate and the air-film interfaces, strongly influencing the optical properties of these VO₂ films. Our optimized single-layered VO₂ films exhibit high integrated luminous transmittance ($T_{lum,l}$ = 43.3%, $T_{lum,h}$ = 39.9%) and solar modulation (ΔT_{sol} = 14.1%, from $T_{sol,l}$ = 42.9% to $T_{sol,h}$ = 28.8%), which are comparable to those of five-layered $TiO_2/VO_2/TiO_2/VO_2/TiO_2$ films ($T_{lum,l}$ = 45%, $T_{lum,h}$ = 42% and ΔT_{sol} = 12%, from $T_{sol,l}$ = 52% to $T_{sol,h}$ = 40%, from *Phys. Status Solidi A-Appl. Mat.* **2009**, *206*, 2155-2160.). Optical calculations suggest that the performance could be further improved by increasing the porosity.

2.5 Optimized optical properties of VO₂-based double or multi-layered films

The current techniques used to improve visible transparency mainly include Mg doping,[95] formation of mixtures (VO₂/SiO₂),[97] regulation of the thickness of VO₂ films[63] and deposition of antireflective layers.[35,52,96] Among these techniques, VO₂-based multi-layered structures containing antireflection layers show better optical performance, especially a

balance between luminous transmittance (T_{lum}) and switching efficiency (ΔT_{sol}). Moreover, the antireflective layer can protect VO_2 from oxidation and add new functions such as photocatalysis.[101,102] ΔT_{lum} represents the improvement of T_{lum} after antireflecion. An integrated improvement of 23 % (from 32 to 55 %) in T_{lum} can be achieved for VO_2/ZrO_2 double layers using ZrO_2 as an antireflective layer.[52] A $TiO_2/VO_2/TiO_2$ three layer shows ΔT_{sol} =2.9 % and ΔT_{lum} = 27% (increased from 31 to 58%).[35] A $TiO_2/VO_2/TiO_2/VO_2/TiO_2$ five layers can improve ΔT_{sol} to 12.1% (6.7 % for the single VO_2 film).[98] All of these films were prepared by gas-phase deposition. And, it seems difficult to improve ΔT_{lum} and ΔT_{sol} simultaneously at a higher ΔT_{lum} level for VO_2 films. The ΔT_{sol} of the $TiO_2/VO_2/TiO_2$ three layer decreased from 3.9 to 2.9 %, while the T_{lum} of the $TiO_2/VO_2/TiO_2/VO_2/TiO_2$ five layer just increased by 4 % (from 41 to 45 %).

The present work was conducted to develop an all-solution preparation process for VO_2-based double-layered films. The study began with the optical optimization of the structure of the double-layered films by combining basic interference principles with spectral
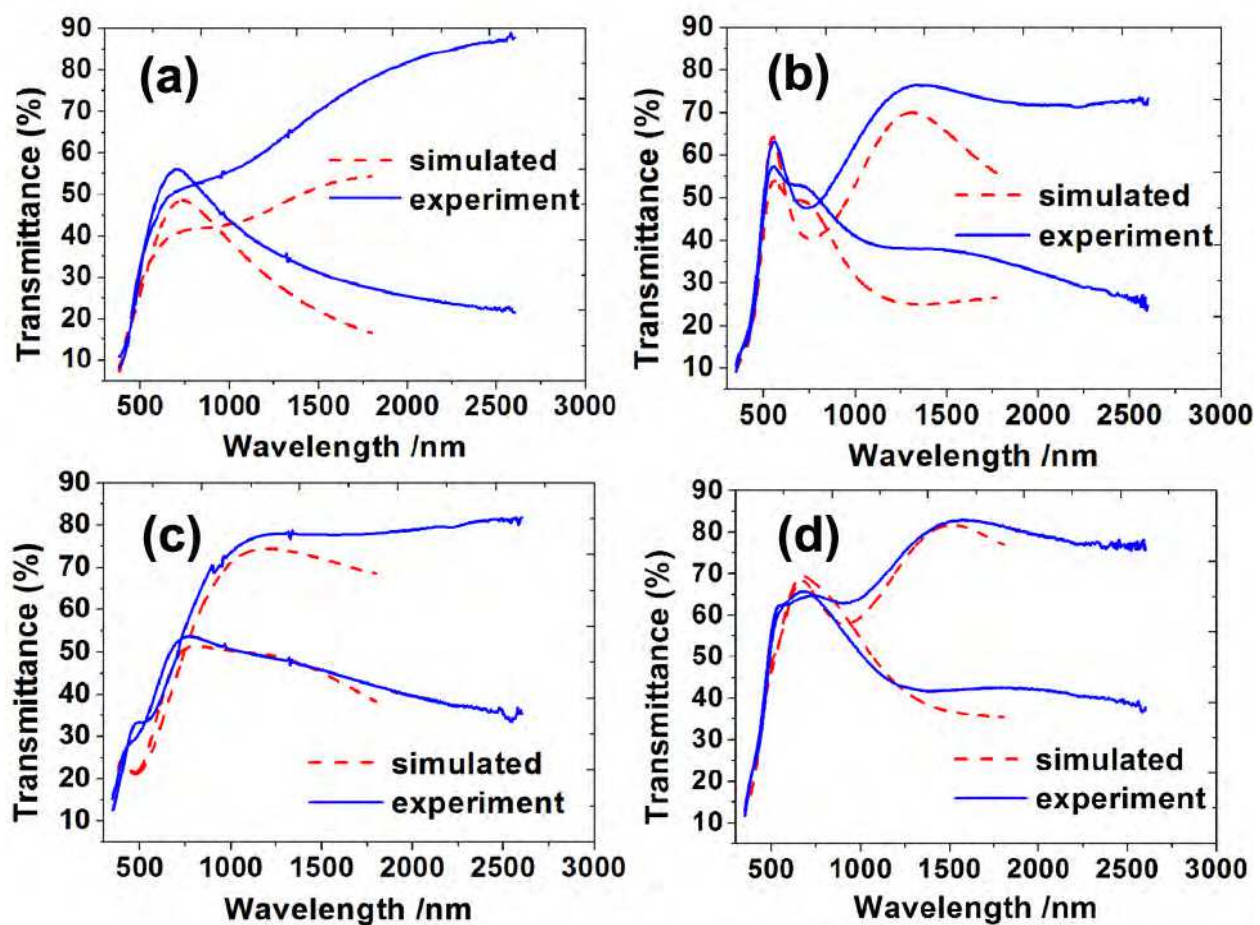

Fig. 23. Simulation and experimental results for various structured VO_2 films. (a) single VO_2(55 nm); (b) VO_2(55 nm)/TiO_2(210 nm) quarter-3-quarter-waved double-layer; (c) VO_2(55 nm)/SiO_2(100 nm)/TiO_2(70 nm) quarter-quarter-quarter triple-layer; (d) VO_2(55 nm)/TiO_2(210 nm)/SiO_2(100 nm) quarter-3-quarter-quarter-waved triple-layer. Data used for simulation: RI of TiO_2 and SiO_2 were 2.5 and 1.45; the thickness for VO_2, quarter-waved TiO_2, 3-quarter-waved TiO_2, and SiO_2 was 45, 56, 168, and 98 nm.[71]

simulation, followed by all-solution preparation and investigation of the improvement in T_{lum} and ΔT_{sol} to confirm the computational predictions. By adding a quarter-waved optical thickness TiO₂ film on VO₂, the integrated luminous reflectance (R_{lum}) of VO₂ was reduced dramatically from 31.2 % to 3.0 %, and T_{lum} is close to that of the TiO₂/VO₂/TiO₂ layer films.[102] These results are comparable to the films prepared by gas-phase deposition,[4, 102] but ΔT_{sol} is slightly higher (6.9 % vs. 6.0 %). In addition, methods to improve ΔT_{sol} while maintaining a high ΔT_{lum} were explored; the highest ΔT_{sol} was 15.1 % for optimised double-layered films, which still showed T_{lum} = 49.5 % at 20 °C and 44.8 % at 90 °C.

The simulation results in **Figure** 23 show that the changing trend of wavelength-dependent transmittance agrees well with the experimental results, and are also similar to the results in the reference.[98] These results suggest that although veracity is not high enough by using optical constants of gas-phase-derived VO₂ films, the simulation still can give a trend prediction on the optical properties.

To improve T_{lum}, the value and position of reflection minima are two key factors. The simulation results show that VO₂ can be simplified as a RI-fixed dielectric film. For a double-
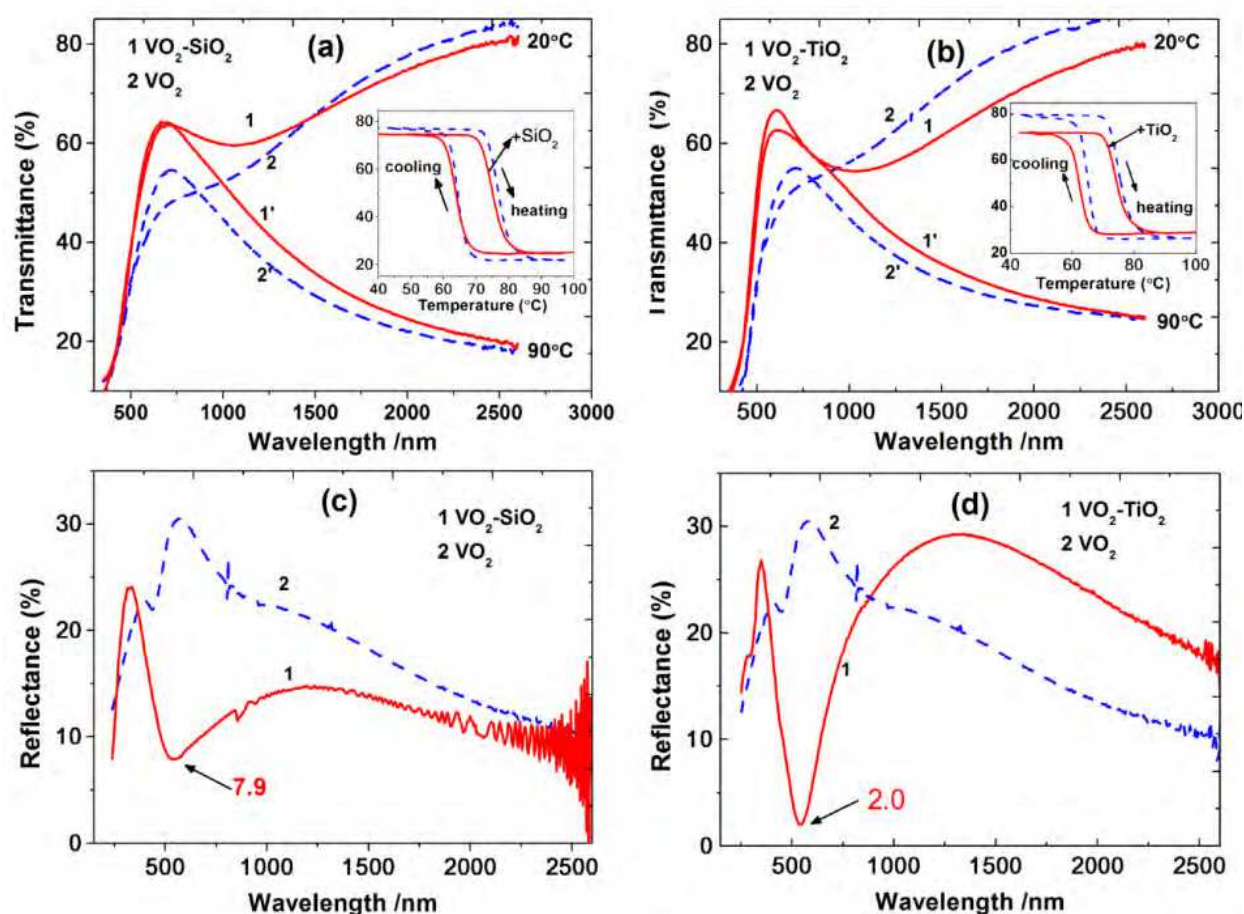

Fig. 24. Transmittance (at 20 and 90 °C) and reflectance (20 °C) spectra before (blue, dotted lines) and after (red, solid lines) adding SiO₂ films (a, c: transmittance and reflectance spectra for sample B2, using SiO₂ as antireflection layer) or TiO₂ films (b, d: transmittance and reflectance spectra for sample B1, using TiO₂ as antireflection layer) on VO₂ films. Insets (a) and (b) are hysteresis loops.[71]

layered film containing two dielectric layers, reflectance minima can be achieved by adjusting the thickness and RI.[103] **Figure** 24 shows the transmittance and reflectance spectra of VO_2/SiO_2 (B2) and VO_2/TiO_2 (B1) double-layered films. Hysteresis loops at 2000 nm before and after coating show that the antireflective coatings have little effects on the thermochromism of VO_2 films. TiO_2 films had a better antireflection efficiency than SiO_2 because the RI of TiO_2 is closer to an ideal value for VO_2.[104] For the simplified VO_2-based double-layered structure, the ideal n_t should be 2.14 to achieve a reflection minimum, n_u (2.6) is the RI of VO_2 in the middle of the visible wavelength range measured by ellipsometry, and n_s (1.45) is the RI of quartz glass. Theoretical simulation results by optical admittance recursive method showed the minimum reflection at 20 °C appearing at n_t=2.10 due to the influence of the extinction coefficient, whereas the minimum R_{lum} (2.8 %, representing luminous reflection) appears at n_t=2.04. For TiO_2, n_t=1.94, the minimum reflectance is 0.5 %, and R_{lum} is 3.0 %; for SiO_2, n_t=1.43, the minimum reflectance is 8.4 %, and R_{lum} is 13.6 %. Experiments results show a reflectance minimum of sample B2 is 7.9 %, and antireflection peaks appeared at 610 nm (20 °C) and 560 nm (90 °C). The minimum reflectance of sample B1 was about 2 % and 4.2 % with antireflection peaks appearing at 560 nm (20 °C) and 520 nm (90 °C). Note that the reflectance is a sum of the values for the film side and the backside of the substrate, actually, the minimum reflectance of the sample on the film side is about 1 % and R_{lum} is about 3.0 %, close to the prediction. R_{lum} of B1 is even lower than that of $TiO_2/VO_2/TiO_2$ three-layer structure sample. A VO_2/SiO_2 double-layered film (sample D, VO_2 thickness is 30 nm) showed enhanced performance (T_{lum} of 78.1 and 76.1 % at 20 and 90 °C, respectively). The highest T_{lum} was shown for a VO_2/TiO_2 double-layered sample, which had T_{lum} of 84.8 %, but ΔT_{sol} (0.9 %) is too small to practically apply. The switching efficiency (ΔT_{sol}) is not only a function of transmittance but also solar energy. Most of the solar energy is distributed in the visible (380-780 nm) and short-wave near-
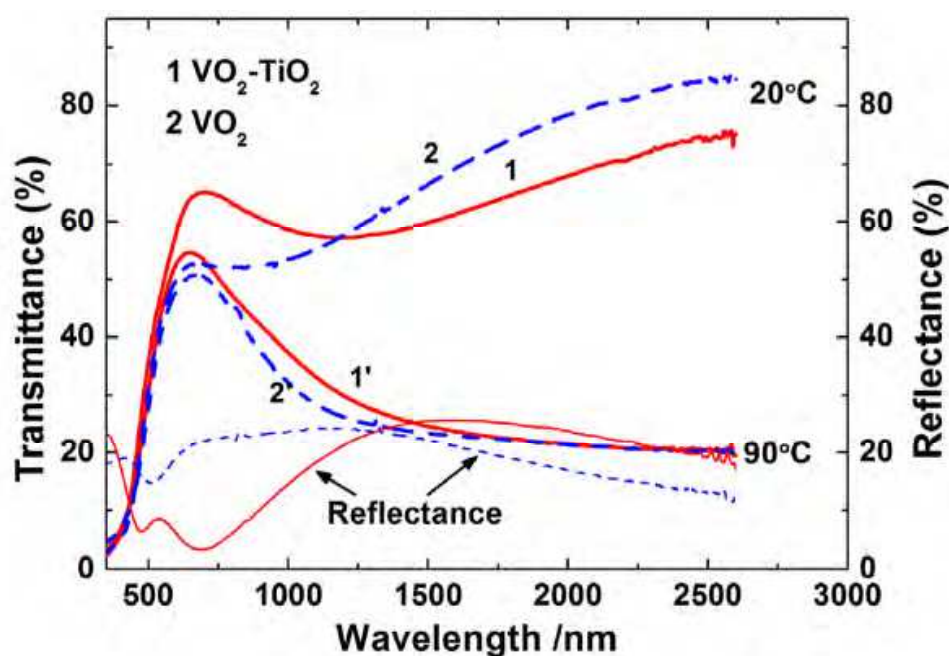

Fig. 25. Transmittance at 20 (1and 2) and 90 °C (1' and 2'), and reflectance spectra (20 °C) of sample A, (95 nm in thickness) without (blue, dotted lines) and with TiO_2 antireflection layer (red, solid lines). [71]

infrared (780-1100 nm) regions. Visible transmittance is almost constant across MIT of VO$_2$ films, so the transmittance difference in the short-wave near-infrared region makes a major contribution to ΔT_{sol}.

One attempt to improve the performance difference at short-wave near-infrared wavelengths is to shift the reflectance minima toward longer wavelengths by regulation of the thickness of antireflective layers. ΔT_{lum} is caused by the different RI of VO$_2$ films at 20 and 90 °C, which influences the value and position of reflectance minima. The half-quarter-waved structure has two reflection minima with one minimum at longer wavelengths, which can improve ΔT_{sol}. The VO$_2$ film (sample A, 95nm) with a 73nm TiO$_2$ antireflective layer gave two antireflection peaks at 20 °C at about 475 nm and 685 nm (**Figure** 25) and led to an increase in ΔT_{sol} of 2.0 %. ΔT_{sol} could be further improved by shifting antireflection peaks to longer wavelengths, but this treatment sacrifices ΔT_{lum} (reflective minimum departure from the middle of visible wavelength range).

To simultaneously increase T_{lum} and ΔT_{sol}, one way is to design an antireflective layer that can form two antireflection peaks both in the visible wavelength range and the short-wave near-infrared wavelength range. For this purpose, a 3-times quarter-waved thick TiO$_2$ (210 nm) film was prepared. Based on the simplified model (using the optical constants of VO$_2$ at 560 nm at 20 °C) two antireflection peaks (correspondingly, two transmittance maxima) should appear at 1680 nm and 560 nm at 20 °C. Experimentally, because the optical constants of VO$_2$ films are wavelength-dependent and existence of extinction coefficient, the first antireflection peak shifted to 1250 nm (20 °C) and 2400 nm (90 °C) (**Figure** 26). However, the second antireflection peak fell in the middle of the visible range (570 and 540 nm for 20 and 90 °C, respectively), and the transmittance difference in the short-wave near-infrared is enlarged due to different ΔT_{lum} at 20 and 90 °C. High ΔT_{lum} values close to those of the quarter-waved samples (17.3 and 11.8 % at 20 and 90 °C) and an improvement of 3.7 % (7.2 to 10.9 %) for ΔT_{sol} were achieved.
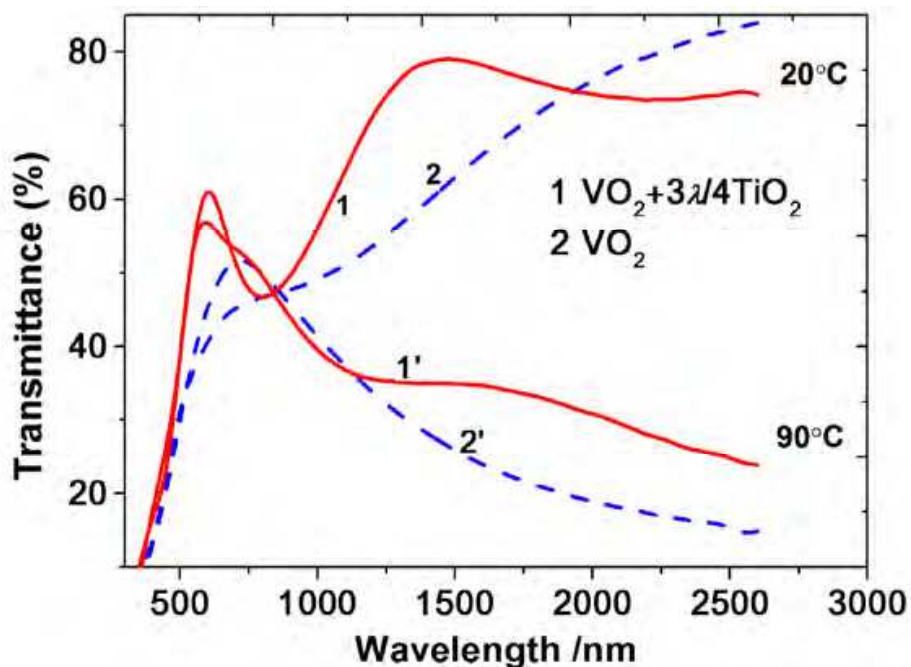

Fig. 26. Transmittance spectra at 20 °C (1, 2) and 90 °C (1', 2') of VO$_2$ film (sample B3) after adding a 3 times quarter-wave thick TiO$_2$ (3λ/4) film (1 and 1').[71]

This work reveals an impressive improvement on the visible transmittance and switching efficiency, and is an important technical breakthrough toward the practical application of VO_2-based smart windows. For a double-layered system, luminous transmittance and switch efficiency could be greatly improved by regulation of the RI and thickness of the films. Single quarter-waved TiO_2 films on VO_2 could reduce R_{lum} from 31.2 to 4.2 %, improving T_{lum} up to 21.2 % at 20 °C (from 40.3 to 61.5 %). Sample with T_{lum} of 78.1 % was further obtained by optimising the thickness of a VO_2 film and adding an antireflective coating, which still had ΔT_{sol} of 7.5 %. The highest ΔT_{sol} achieved was 15.1 %. Films with balanced luminous transmittance (T_{lum}=58.0 and 53.9 % at 20 and 90 °C, respectively) and switching efficiency (10.9 %) were prepared.

3. Summary remarks and outlook

This chapter introduces a solution method, polymer assisted deposition process, for the preparation of VO_2 and VO_2-based multilayered films. The method enables us to facially control over the film thickness, morphology and optical constants. By combining the optical design in respect to the materials selection and/or their thickness and microstructural control, we obtained VO_2 films with high visible transmittance (40-84%), controllable Mott phase transition temperatures and high switching efficiencies (max. 15.1%). The results show that the current solution process is a powerful competitor towards practical applications of this material.

4. Acknowledgements

5. References

[1] Parkin, I. P.; Manning, T. D. *J. Chem. Educ.* 2006, *83*, 393.
[2] Irie, M. *Chem. Rev.* 2000, *100*, 1685.
[3] Maaza, M.; Bouziane, K.; Maritz, J.; McLachlan, D. S.; Swanepool, R.; Frigerio, J. M.; Every, M. *Opt. Mate.* 2000, *15*, 41.
[4] Jin, P.; Xu, G.; Tazawa, M.; Yoshimura, K. *Jpn. J. Appl. Phys.* 2002, *41*, L278.
[5] Mlyuka, N. R.; Niklasson, G. A.; Granqvist, C. G. *Sol. Energ. Mat. Sol. Cells.* 2009, *93*, 1685.
[6] Lee, M. J.; Park, Y.; Suh, D. S.; Lee, E. H.; Seo, S.; Kim, D. C.; Jung, R.; Kang, B. S.; Ahn, S. E.; Lee, C. B.; Seo, D. H.; Cha, Y. K.; Yoo, I. K.; Kim, J. S.; Park, B. H. Adv. Mater. 2007, *19*, 3919.
[7] Baek, I. G.; Kim, D. C.; Lee, M. J.; Kim, H. J.; Yim, E. K.; Lee, M. S.; Lee, J. E.; Ahn, S. E.; Seo, S.; Lee, J. H.; Park, J. C.; Cha, Y. K.; Park, S. O.; Kim, H. S.; Yoo, I. K.; Chung, U.

I.; Moon, J. T.; Ryu, B. I.; Ieee. In *Ieee International Electron Devices Meeting 2005, Technical Digest*, 2005; 769.

[8] Morin, F. J.; *Phys. Rev. Lett.* 3 (1959) 34-36.

[9] Manning, T. D.; Parkin, I. P.; Clark, R. J. H.; Sheel, D.; Pemble, M. E.; Vernadou, D.; *J. Mater. Chem.* 12 (2002) 2936-2939.

[10] Cavalleri, A.; Tóth, C.; Siders, C. W.; Squier, J. A.; Ráksi, F.; Forget, P.; Kieffer, J. C.; *Phys. Rev. Lett.* 87 (2001) 237401,1-4.

[11] Baum, P.; Yang, D. S.; Zewail, A. H. *Science* 2007, *318*, 788.

[12] Lysenko, S.; Rua, A.; Vikhnin, V.; Fernandez, F.; Liu, H. *Phys. Rev. B* 2007, *76*.

[13] Cavalleri, A.; Rini, M.; Chong, H. H. W.; Fourmaux, S.; Glover, T. E.; Heimann, P. A.; Kieffer, J. C.; Schoenlein, R. W. *Phys. Rev. Lett.* 2005, *95*, 067405.

[14] Becker, M. F.; Buckman, A. B.; Walser, R. M.; Lepine, T.; Georges, P.; Brun, A. *J. App. Phys.* 1996, *79*, 2404.

[15] Beteille, F.; Livage, J. *J. Sol-Gel Sci. Technol.* 1998, *13*, 915.

[16] Guzman, G.; Beteille, F.; Morineau, R.; Livage, J. *J. Mater. Chem.* 1996, *6*, 505.

[17] Livage, J. *Solid State Ionics* 1996, *86 (8)*, 935-942.

[18] Nag, J.; Haglund, R. F. *Journal of Physics-Condensed Matter* 2008, *20*, 264016.

[19] Balu, R.; Ashrit, P. V. *Applied Physics Letters* 2008, *92*, 021904.

[20] Andersson.G. *Acta Chem. Scand.* 1954, *8*, 1599.

[21] Andersson, G. *Acta Chem. Scand.* 1956, *10*, 653.

[22] Matsuishi.T. *Jpn. J. Appl. Phys* 1967, *6*, 1060.

[23] Oka, Y.; Yao, T.; Sato, S.; Yamamoto, N. *J. Solid State Chem* 1998, *140*, 219.

[24] Théobald, F. *J. Less-CommonMet* 1977, *53*, 55.

[25] Galy, J. *J.Solid State Chem* 1999, *148*, 224.

[26] Oka, Y. *J. Solid State Chem.* 1990, *86*, 116.

[27] Hagrman, D.; Zubieta, J.; Warren, C. J.; Meyer, L. M.; Treacy, M. M. J.; Haushalter, R. C. *J.Solid State Chem* 1998, *138*, 178.

[28] Gui, Z.; Fan, R.; Chen, X. H.; Wu, Y. C. *J. Solid State Chem* 2001, *157*, 250.

[29] Liu, C. H.; Zapien, J. A.; Yao, Y.; Meng, X. M.; Lee, C. S.; Fan, S. S.; Lifshitz, Y.; Lee, S. T. *Adv Mater* 2003, *15*, 838.

[30] Qazilbash, M. M.; Schafgans, A. A.; Burch, K. S.; Yun, S. J.; Chae, B. G.; Kim, B. J.; Kim, H. T.; Basov, D. N. *Phys. Rev. B* 2008, *77*, 115121.

[31] Verleur, H. W.; Barker, A. S.; Berglund, C. N. *Phys. Rev. Lett* 1968, *172*, 788.

[32] Manning, T. D.; Parkin, I. P.; Pemble, M. E.; Sheel, D.; Vernardou, D. *Chem. Mater* 2004, *16*, 744-749.

[33] Burkhardt, W.; Christmann, T.; Franke, S.; Kriegseis, W.; Meister, D.; Meyer, B. K.; Niessner, W.; Schalch, D.; Scharmann, A. *Thin Solid Films* 2002, *402*, 226-231.

[34] Jin, P.; Tanemura, S. *Jpn. J. Appl. Phys., Part 1* 1994, *33*, 1478-1483.

[35] Jin, P.; Xu, G.; Tazawa, M.; Yoshimura, K. *Appl. Phys. A* 2003, *77*, 455-459.

[36] Binions, R.; Hyett, G.; Piccirillo, C.; Parkin, I. P. *J. Mater. Chem* 2007, *17*, 4652-4660.

[37] Takahashi, I.; Hibino, M.; Kudo, T. *Jpn. J. Appl. Phys., Part 1* 2001, *40*, 1391-1395.

[38] Manning, T. D.; Parkin, I. P. *J. Mater. Chem* 2004, *14*, 2554-2559.

[39] Vernardou, D.; Pemble, M. E.; Sheel, D. W. *Chem. Vap. Deposition* 2007, *13*, 158-162.

[40] Sobhan, M. A.; Kivaisi, R. T.; Stjerna, B.; Granqvist, C. G. *Sol. Energy Mater. Sol. Cells* 1996, *44*, 451-455.

[41] Blackman, C. S.; Piccirillo, C.; Binions, R.; Parkin, I. P. *Thin Solid Films* 2009, *517*, 4565-4570.

[42] Guinneton, F.; Sauques, L.; Valmalette, J. C.; Cros, F.; Gavarri, J. R. *J. Phys. Chem. Solids* 2001, *62*, 1229-1238.

[43] (a) Kang, L. T.; Gao, Y. F.; Luo, H. J. *ACS Appl. Mater. Interfaces* 2009, *1*, 2211-2218. (b) Kang, L. T.; Gao, Y. F.; Luo, H. *Materials Science Forum*, 2011, 687, 791

[44] Kang, L. T.; Gao, Y. F.; Zhang Z. T.; Du J.; Cao, C. X.; Chen, Z.; Luo, H. J. *J. Phys Chem C.* 2010, *114 (4)*, 1901–1911.

[45] Guinneton, F.; Sauques, L.; Valmalette, J. C.; Cros, F.; Gavarri, J. R. *Thin Solid Films* 2004, *446*, 287-295.

[46] Xu, G.; Jin, P.; Tazawa, M.; Yoshimura, K. *J. Appl. Phys., Part 1* 2004, *43*, 186-187.

[47] Chen, B.; Yang, D. F.; Charpentier, P. A.; Zeman, M. *Sol. Energy Mater. Sol. Cells* 2009, *93*, 1550-1554.

[48] Guinneton, F.; Sauques, L.; Valmalette, J. C.; Cros, F.; Gavarri, J. R. *J. Phys. Chem. Solids* 2005, *66*, 63-73.

[49] Brassard, D.; Fourmaux, S.; Jean-Jacques, M.; Kieffer, J. C.; El Khakani, M. A. *Appl. Phys. Lett* 2005, *87*, 051910

[50] Griffiths, C.H.; Eastwood, H. K. *J. Appl. Phys* 1974, 2201-2206.

[51] Kusano, E.; Theil, J. A. *J. Vac. Sci. Technol., A* 1989, *7*, 1314-1317.

[52] Xu, G.; Jin, P.; Tazawa, M.; Yoshimura, K. *Sol. Energy Mater. Sol. Cells* 2004, *83*, 29-37.

[53] Lappalainen, J.; Heinilehto, S.; Saukko, S.; Lantto, W.; Jantunen, H. *Sens. Actuators, A* 2008, *142*, 250-255.

[54] Chain, E.E.; *Appl. Opt.*, 1991, 30, 2782-2787.

[55] Choi, H.S.; Ahn, J.S.; Jung, J.H.; Noh, T.W.; Kim, D.H.; *Phys. Rev. B: Condens. Matter Mater. Phys*, 1996, 54, 4621-4628.

[56] Lopez, R.; Boatner, L.A.; Haynes, T.E.; Feldman, L.C.; Haglund, R.F.; *J. Appl. Phys.*, 2002, 92, 4031-4036.

[57] Narayan, J.; Bhosle, V.M.; *J. Appl. Phys.*, 2006, 100, 103524.

[58] Petit, C.; Frigerio, J.M.; Goldmann, M.; *J. Phys.: Condens. Matter*, 1999, 11, 3259-3264.

[59] Kakiuchida, H.; Jin, P.; Tazawa, M.; *Sol. Energy Mater. Sol. Cells*, 2008, 92, 1279-1284.

[60] Cao, C.; Gao, Y.-F.; Luo, H.J.; *J. Phys. Chem. C*, 2008, 112 (48), 18810–18814.

[61] Bai,L. Y.; Gao, Y. F.; Li，W. D.; Luo, H. J.; Jin, P.; *J. Ceram. Soc. Japan*, 2008, 116(3), 395-399 .

[62] Zhang, Z.; Gao, Y. F.; Chen, Z.; Du, J.; Cao, C.; Kang L. T.; Luo, H.J.; *Langmuir*，2010, 26 (13), 10738–10744.

[63] Kang, L. T.; Gao, Y. F.; Chen, Z.; Du, J.; Zhang Z.; Luo, H.J.; *Sol. Energy Mater. Sol. Cells*, 2010, 94, 2078–2084.

[64] Du, J.; Gao, Y. F.; Luo, H. J.; Kang, L. T.; Chen, Z.; Zhang Z.; Cao, C.; *Sol. Energy Mater. Sol. Cells*, 2011, 95 (2), 469-475.

[65] Cao, C.; Gao, Y. F.; Kang, L. T.; Luo, H. J.; *CrystEngComm*, 2010, 12 (12), 4048 – 4051.

[66] Dai, L.; C.; Gao, Y. F.; Luo, H. J.; *Sol. Energy Mater. Sol. Cells*, 2011, 95 (2), 712-715.

[67] Zhang, Z.; Gao, Y. F.; Kang L. T.; Du, J.; Luo, H.J.; *J. Phys. Chem. C*, 2010, *114,* 22214–22220.

[68] Du, J.; Gao, Y. F.; Luo, H. J.; Zhang Z.; Kang, L. T.; Chen, Z.; *Sol. Energy Mater. Sol. Cells*, 2011, 95, 1604-1609.

[69] Kang, L. T.; Gao, Y. F.; Chen, Z.; Du, J.; Zhang Z.; Luo, H.J.; *ACS Applied Materials & Interfaces*, 2011, *3(2)*, 135-138.

[70] Ni, J.; Jiang, W.; Yu, K.; Gao, Y. F.; Zhu, Z.; *Electrochimica Acta,* 2011, 56, 2122-2126.

[71] Chen, Z.; Gao, Y. F.; Kang, L. T.; Du, J.; Zhang Z.; Luo, H. J.; Miao, H.; Tan, G.; *Sol. Energy Mater. Sol. Cells*, 2011, 95(9), 2677-2684.

[72] Kang, L. T.; Gao, Y. F.; Luo, H.J.; Wang, J.; Zhu, B.; Zhang Z.; Du, J.; Kanehira, M.; Zhang, Y.; Thermochromic Properties and Low Emissivity of ZnO:Al/VO₂ Double-Layered Films with a Lowered Phase Transition Temperature, *Sol. Energy Mater. Sol. Cells*, in press.

[73] Yuan, X. P.; Li, C. C.; Guan, G. H.; Xiao, Y. N.; Zhang, D. *J. Appl. Polym. Sci.* 2009, 111, 566–575.

[74] Wang, Z. D.; Xu, Z. L.; Yang, Y. G.; Li, S. X. *Mater. Rev. (Chongqing, P. R. China) Special Issue VII,* 2006, 20, 53–57 (in Chinese).

[75] Hao, C. W.; Zhao, Y.; Zhou, Y.; Zhou, L. J.; Xu, Y. Z.; Wang, D. J.; Xu, D. F. *J. Polym. Sci., Part B: Polym. Phys.* 2007, 45, 1589–1598.

[76] Kim, J. H.; Kim, C. K.; Won, J.; Kang, Y. S. *J. Membr. Sci.* 2005, 250, 207–214.

[77] Kim, J. H.; Min, B. R.; Won, J.; Kang, Y. S. *Chem.sEur. J.* 2002, 8, 650–654.

[78] Hong, S. U.; Jin, J. H.; Won, J.; Kang, Y. S. *Adv. Mater.* 2000, 12, 968–971.

[79] Kim, H. T.; Chae, B. G.; Youn, D. H.; Kim, G.; Kang, K. Y.; Lee, S. J.; Kim, K.; Lim, Y. S. *Appl. Phys. Lett.* 2005, 86, 242101.

[80] Petrov, G. I.; Yakovlev, V. V.; Squier, J. *Appl. Phys. Lett.* 2002, 81, 1023–1025.

[81] Shi, J. Q.; Zhou, S. X.; You, B.; Wu, L. M. *Sol. Energy Mater. Sol. Cells* 2007, 91, 1856–1862.

[82] Lopez, R.; Haynes, T. E.; Boatner, L. A.; Feldman, L. C.; Haglund, R. F. *Phys. Rev. B* 2002, 65, 224113.

[83] Suh, J. Y.; Lopez, R.; Feldman, L. C.; Haglund, R. F. *J. Appl. Phys.* 2004, 96, 1209–1213.

[84] Klimov, V. A.; Timofeeva, I. O.; Khanin, S. D.; Shadrin, E. B.; Ilinskii, A. V.; Silva-Andrade, F. *Tech. Phys.* 2002, 47 (9), 1134–1139.

[85] Frenzel, A.; Qazilbash, M. M.; Brehm, M.; Chae, B. G.; Kim, B. J.; Kim, H. T.; Balatsky, A. V.; Keilmann, F.; Basov, D. N. *Phys. ReV. B* 2009, 80 (11), 115115.

[86] Aliev, R. A.; Klimov, V. A. *Phys. Solid State* 2004, 46 (3), 532– 536.

[87] Aliev, R.; Andreev, V.; Kapralova, V.; Klimov, V.; Sobolev, A.; Shadrin, E. *Phys. Solid State* 2006, 48 (5), 929–934.

[88] Whittaker, L.; Jaye, C.; Fu, Z. G.; Fischer, D. A.; Banerjee, S. *J. Am. Chem. Soc.* 2009, 131 (25), 8884–8894.

[89] Donev, E. U.; Lopez, R.; Feldmant, L. C.; Haglund, R. F. *Nano Lett.* 2009, 9 (2), 702–706.

[90] Muraoka, Y.; Hiroi, Z. *Appl. Phys. Lett.* 2002, 80 (4), 583–585.

[91] Jia, Q. X.; McCleskey, T. M.; Burrell, A. K.; Lin, Y.; Collis, G. E.; Wang, H.; Li, A. D. Q.; Foltyn, S. R. *Nat. Mater.* 2004, 3 (8), 529–532.

[92] Kingery, W. D. *Introduction To Ceramics*; John Wiley and Sons, Inc.: New York, 1960.

[93] Lopez, R.; Boatner, L. A.; Haynes, T. E.; Haglund, R. F.; Feldman, L. C. *Appl. Phys. Lett.* 2001, 79 (19), 3161–3163.

[94] Sidorov, A. I.; Vinogradova, O. P.; Obyknovennaya, I. E.; Khrushchova, T. A. *Tech. Phys. Lett.* 2007, 33 (7), 581–582.

[95] Mlyuka, N.R.; Niklasson, G.A.; Granqvist, C.G. *Appl. Phys. Lett.*, 2009, 95, 171909.

[96] Lee, M.H. Cho, J.S. *Thin Solid Films*, 2000, 365, 5-6.

[97] H.-K. Chen, H.-C. Hung, T.C.K. Yang, S.-F. Wang, *J. Non-Cryst. Solids*, 2004, 347, 138-143.

[98] N.R. Mlyuka, G.A. Niklasson, C.G. Granqvist, *Physica Status Solidi a-Applications and Materials Science*, 2009, 206, 2155-2160.

[99] Li, S.-Y.; Niklasson, G. A.; Granqvist, C. G. *J. Appl. Phys.* 2010, 108, 063525.

[100] Lu, C. L.; Cheng, Y. R.; Liu, Y. F.; Liu, F.; Yang, B. *Adv. Mater.* 2006, 18, 1188–1192.

[101] P. Evans, M.E. Pemble, D.W. Sheel, H.M. Yates, *J. Photochem. Photobiol. A-Chem.*, 2007, 189, 387-397.

[102] Saitzek, S.; Guinneton, F.; Sauques, L.; Aguir, K.; Gavarri, J.R.; *Opt. Mater.*, 2007, 30, 407-415

[103] Heavens, O.S. *Optical Properties of Thin Solid Films*, Courier Dover Publications, 1991.

[104] Babulanam, S.M.; Eriksson, T.S.; Niklasson, G.A.; Granqvist, C.G. *Solar Energy Materials*, 1987, 16, 347-363.
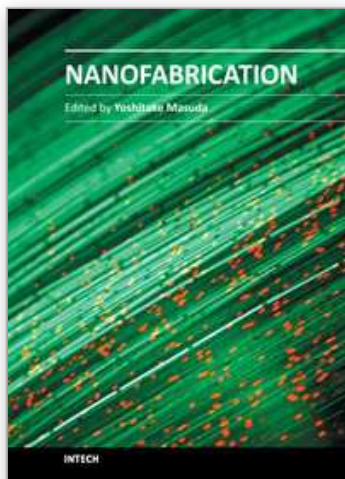
Nanofabrication

Edited by Dr. Yoshitake Masuda

We face many challenges in the 21st century, such as sustainably meeting the world's growing demand for energy and consumer goods. I believe that new developments in science and technology will help solve many of these problems. Nanofabrication is one of the keys to the development of novel materials, devices and systems. Precise control of nanomaterials, nanostructures, nanodevices and their performances is essential for future innovations in technology. The book "Nanofabrication" provides the latest research developments in nanofabrication of organic and inorganic materials, biomaterials and hybrid materials. I hope that "Nanofabrication" will contribute to creating a brighter future for the next generation.

How to reference

In order to correctly reference this scholarly work, feel free to copy and paste the following:

Yanfeng Gao, Litao Kang, Zhang Chen and Hongjie Luo (2011). Solution Processing of Nanoceramic VO2 Thin Films for Application to Smart Windows, Nanofabrication, Dr. Yoshitake Masuda (Ed.), ISBN: 978-953-307-912-7, InTech, Available from: http://www.intechopen.com/books/nanofabrication/solution-processing-of-nanoceramic-vo2-thin-films-for-application-to-smart-windows

INTECH
open science | open minds